

THE OXIDATION OF NiAl: What Can We Learn from Ab Initio Calculations?

M.W. Finnis,¹ A.Y. Lozovoi,¹ and A. Alavi²

¹*School of Mathematics and Physics, Queen's University Belfast, Belfast BT7 1NN, Northern Ireland, United Kingdom; email: m.finnis@qub.ac.uk, s.lozovoi@qub.ac.uk*

²*Chemistry Department, University of Cambridge, Lensfield Road, Cambridge CB2 1EW, United Kingdom; email: asa10@cam.ac.uk*

Key Words ordered compounds, selective oxidation, point defects, environmental parameters

■ **Abstract** We review here the theory of the early stages of oxidation of the (110) surface of $\text{Ni}_{1-x}\text{Al}_x$, based on ab initio calculations using a plane-wave pseudopotential method. The clean surface and several oxidized surfaces have been investigated, with oxygen coverages up to 2 ML of oxygen (1 ML = 3 O atoms per 2 surface Al atoms). The theory to date is a description in terms of equilibrium thermodynamics, with a comparison of the free energies of several surfaces of different composition, implemented at the atomic scale. Three environmental parameters are singled out as control variables in this treatment, namely the alloy composition x (assumed to be near 0.5), the temperature T and the partial pressure of oxygen p_{O_2} . With certain reasonable approximations an analytic formula for the surface energy σ is derived in terms of these variables and some constants that are calculated ab initio together with others that are derived from experimental thermodynamic tables. At oxygen pressures just above the threshold for bulk oxidation of NiAl, the calculations explain the observed formation of a thin film of alumina in place of NiAl surface layers, with the consequent dissolution of Ni into the bulk. Ab initio calculations illustrate how the energetics of supplying Al to the surface depends on bulk stoichiometry, which alters the relative stability of different surface oxidation states so as to favour oxidation more if the alloy is Al-rich than if it is Ni-rich.

INTRODUCTION

We now recognize that the oxidation of materials, once considered a problem similar to other kinds of corrosion, can sometimes be a process of enormous value. Silicon dioxide films for example are still at the heart of the electronics industry and will be for many years to come because they are the simplest useful gate oxides. One might well ask where that industry would be if silicon oxidized in the uncontrollable manner of iron. At the another extreme, aluminum oxide films occur spontaneously, not only on aluminum itself, but on many useful

aluminum-containing alloys, including NiAl. These films are protective because they are relatively stable and continuous, and hence they are desirable, for example on turbine blades in power generation, or other components subject to high temperature corrosive environments (1). Their morphology and rate of growth are still rather poorly understood from a fundamental point of view. Such films can also play a quite different role, by acting as substrates for deposited films of other, catalytic materials (2). In this review we focus on NiAl as a well studied example.

Our purpose here is to illustrate how *ab initio* calculations can be used effectively to predict the relative stability of various oxidized surface structures as a function of externally imposed thermodynamic parameters (referred to here as environmental parameters), such as temperature, oxygen partial pressure, and chemical composition of the substrate. This latter aspect, in particular, adds considerable richness to the problem. Unlike elemental systems, our chosen substrate, being a two-component compound, has the freedom to vary the chemical composition of the surface layer (and more generally the surface region) as the oxidation proceeds: The compound will do so if it can lower its free energy (i.e., its surface excess free energy). This can lead to enrichment of the surface region with one of the components, thus exhibiting selective oxidation. This enrichment, in turn, requires the mass transport of material to and from the bulk. Therefore, the oxidation process at the surface becomes intimately related to bulk thermodynamics and kinetics in a manner whose description goes well beyond the standard treatment of oxidation processes of elemental systems. In particular, we show that the bulk point-defect behavior of NiAl is an essential physical ingredient. Furthermore, we show that the extension of the *ab initio* thermodynamic formalism, combined with the theory of point defects in NiAl, is a framework in which this selective oxidation process can be studied.

Considering oxidation at an atomistic level, one would hope to address at least three questions: (a) How would the oxidation proceed? (b) What is the rate of oxidation? (c) What is the final structure at which the system arrives? It is generally assumed that there is an initial, transient phase during which the first layer or layers of oxide are created, merging into a steady-state phase during which bulk diffusion events and interface reactions can be distinguished, one of which may be rate-determining. In steady state, the presence of grain boundaries in the oxide film and interface roughness, as well as the development and relief of stresses in the oxide film are complications that would make a fully atomistic simulation out of reach of current techniques, and thus continuum mechanics and diffusion theory would be the tools of choice. By studying the early stages of oxidation, however, or investigating particular events at any stage, *ab initio* calculations can now contribute to our understanding.

To answer the first question, an extreme and naive approach would be to try to monitor the evolution of the System, for example, by running a molecular dynamics (MD) simulation. Some accelerated way to do this (3) would be necessary, otherwise it would take unacceptably long for a single vacancy simply to jump into a neighboring site. Nevertheless, such an approach would be a formidable

challenge to present computational resources, unless one used such a drastically simplified model of interatomic interactions that the computed outcomes would be of questionable value. This is not to say that the MD technique is of no value for any oxidation studies at present; on the contrary, in specific cases it might lead to results that would be hard to achieve in any other way. An impressive example is the study of the oxidation of Al(111) (4), which demonstrated that the energy released during the adsorption and dissociation of an O₂ molecule is sufficient to initiate the local precursor of an oxide phase, at an oxygen coverage as low as 0.5 ML.

An alternative approach, which is the method of choice in most oxidation studies, is to identify a number of consecutive atomic structures through which the system proceeds during the oxidation process. This approach relies on our intuition and even luck in selecting structures worth considering, so it is very much modeling rather than simulation, but it offers a much better ratio of insight to computation than does brute force MD. Given that the number of possible structures grows exponentially with the number of atoms in the model, the final result can be no more than a best-educated guess, no matter how accurate the calculations. The studies of oxidation based on first-principles calculations, which have started to appear in recent years, have therefore concentrated on low-index surfaces of single-component crystals. The systems considered are either late transition and noble metals (5–15), where the formation enthalpy of the oxides is relatively low, or metals that form highly stable oxides such as Mg (16, 17) and Al (18, 19). In the former, the oxidation typically proceeds through a number of ordered structures of the adsorbed oxygen (14, 20) and eventually begins introducing oxygen sub-surface (15). Soon after that the surface oxide starts to resemble a stack of ordered oxygen-metal layers, which continues to thicken as more oxygen atoms arrive, subject to kinetic restrictions. On Mg(0001), on the other hand, oxygen atoms go straight under the surface layer (16). Oxygens tend to group together forming oxide islands (17), which grow laterally until the whole surface is covered. Oxidation of Al(111) is a little more complicated. The introduction of subsurface oxygens becomes energetically favorable only after 1 ML of oxygen atoms has settled on the surface. However, the same tendency of oxygen atoms to cluster together promotes oxide nucleation long before an average oxygen coverage of 1 ML is reached (18, 19). The oxide islands then continue to grow laterally, as on Mg(0001). In order to identify the system's oxidation path and the rate of oxidation (the second question), one needs not only to find out the sequence of surface structures through which the oxidizing system might pass, but also to calculate the energetic barriers separating these structures from each other. The search for saddle points on the energy surface is a time-consuming task, and to our knowledge has not been accomplished for the oxidation process for any metals. Fortunately, the elucidation of the exact sequence of atomic jumps occurring at and near the particular oxidizing surface is not really the only answer in which one is interested. It is also useful to understand the energy differences that drive the system through a particular path.

Recent groundbreaking work on calculating energy barriers for the oxidation of Si (21) illustrates the current state of the art in ab initio simulation. This study

also shows the difficulties that still must be overcome even for single-component substrates. The authors created an ensemble of amorphous oxide structures on Si using classical interatomic potentials, and they relaxed these structures with an ab initio (density functional) code. They then studied in detail how a single oxygen molecule arriving at the interface would dissociate, breaking open the Si lattice and bonding to the Si. This was achieved by dragging the molecule to the interface, relaxing all the atomic positions to their minimum energy configuration at each stage on the journey. Note that a fully dynamic simulation of the inward diffusion of the molecule would have been too time consuming. Despite its size limitations, this model was clearly able to provide new insights, notably that oxygen dissociation and incorporation presents no significant energy barrier and is spontaneous when the molecule has arrived at the interface. Such a procedure for a multicomponent substrate, even for NiAl, would be considerably more difficult, because oxygen not only must diffuse to the interface, aluminum must be there to meet it, so a sequence of processes, or cooperative processes, must be identified. However, that is not to say it would be impossible, and this process represents another general strategy for future consideration.

The answer to the third question is again a matter of kinetics. Unless the temperature is very high or the partial pressure of oxygen is very low, thermodynamic equilibrium is not attained until the entire metal has become an oxide or a combination of oxides. This can be easily appreciated by comparing the heat of formation of NiAl, $H_f(\text{NiAl}) = -61.8 \text{ kJ/mol}$ (22) with those of the respective oxides, $H_f(\text{NiO}) = -489.5 \text{ kJ/mol}$, and $H_f(\text{Al}_2\text{O}_3) = -1675.7 \text{ kJ/mol}$ (23). For some noble and late transition metals, a thin oxide film may appear to be of lower energy than the equivalent amount of bulk oxide (6, 10, 13); however, the metal is still unstable against further oxidation. In practical terms this means that for any model of an oxidized surface constructed in the laboratory, another structure with lower free energy always exists, which could be created by adding more oxygen atoms. However, the timescale for further oxidation may be much longer than the timescale for attaining and equilibrating the oxide layer at its current thickness. Hence, any particular structure is at best metastable, but this is the normal situation in thermodynamics; one can make satisfactory predictions by excluding any states that are inaccessible on the timescales of interest. With this in mind, the general strategy we and others (10–14) have followed for predicting equilibrium configurations and free energies can be stated as follows: One calculates the interfacial excess Gibbs free energy for each structure of a finite set, which must be locally stable; that is, all the atomic coordinates are relaxed to equilibrium, although globally the system is only metastable. This set contains a manageable number of trial stoichiometries and atomic configurations, of order perhaps 10–100. It cannot be exhaustive but it should be representative. The best prediction of the structure will be the one in this set having the lowest excess Gibbs free energy. A key role in this analysis is played by the chemical potentials of the components, upon which the excess Gibbs free energies depend. Chemical potential is inherently a nonlocal property; that is, the chemical potential of a species of atom does not depend on

any atom's immediate environment but on the system as a whole. The chemical potentials are computed separately from bulk calculations, and therefore they enter the expression for the excess Gibbs energy of a surface film a posteriori, after the detailed and time-consuming atomistic simulations of the surface have been made. This greatly extends the analysis because approximate calculations of excess Gibbs free energy versus temperature and versus chemical potential of the components can be made easily to reveal the limits of stability of a particular structure.

In the case of NiAl(110), the initial oxidation results in a continuous thin aluminum oxide film. According to the suggested structural model of the film (24, 25), it consists of two O–Al bilayers with every 3 oxygen atoms in each bilayer roughly corresponding to 2 aluminum atoms in a layer of the substrate. Hence, to model the initial oxidation of a NiAl(110) surface it suffices to consider the oxygen coverage up to 2 ML (1 ML = 3 O atoms per every 2 surface Al atoms). The following sections describe how the excess Gibbs free energy of the surface in its early stages of oxidation has been calculated as a function of the temperature, the stoichiometry of the metal, and the p_{O_2} . We hope to make clear how the same approach can be applied to other systems and how it can be improved and extended to make use of faster computers.

THEORY

In the following sections we outline the theory of the excess Gibbs free energy (for short: the surface energy) σ of a planar surface of arbitrary thickness at the atomistic level and explain how σ can be calculated by making use of ab initio total energy results for internal energies at 0 K. Surface energies of oxidized surfaces are very sensitive to temperature, and to the chemical potentials of the components including oxygen itself, which is why the ab initio internal energies are just one part of the story. Vibrational contributions are usually neglected in surface energy calculations, as they have been in studies of oxidation to date. On the other hand more important variations with temperature occur owing to the temperature dependence of the chemical potentials of the components, and these can be included analytically. The chemical potential of each component can be expressed in terms of its partial pressure (most appropriate for oxygen, or other naturally gaseous species) or solid concentration (most appropriate for alloy components or impurities). The latter step requires proper acknowledgment of the fact that the zero of chemical potential in atomistic models of the energy is different to the zero employed in chemistry.

The advantages of the approach just summarized have been widely appreciated. It has been referred to as ab initio thermodynamics (26–28) or first-principles atomistic thermodynamics (29), and it is currently used by a number of independent research groups. For example, the oxidation of the Ag, Rh, Pt, and Pd surfaces has recently been investigated using the above technique (10–14). It has now been applied for studying the equilibrium structure of several oxide surfaces: Cr₂O₃(0001)

(30), Fe₂O₃(0001) (28), V₂O₅(0001) (31), ZnO(0001) (32), RuO₂(110) (33), and various surfaces of PdO (29) and α -Al₂O₃ (34–38).

Below we outline the approach in terms of surface excesses of the components (39), which makes the effect of non-stoichiometry at the surface explicit. Throughout we refer to NiAl as an illustration. For more detailed descriptions in other contexts the reader is referred to these references (5–19, 26–38, 40, 41). The formulae are readily applied to other systems.

Thermodynamics at the Atomic Scale

Our formulation of the surface energy is based on that of Cahn's (39) for homogeneous substances, which was generalized previously to multi-component crystals (42). The system we consider is always an infinite slab some tens of atomic planes in thickness, which is the kind of atomistic system that is simulated in most calculations. Three-dimensional periodic boundary conditions are applied to a piece of the slab, with a vacuum separating it typically by one nanometer from its periodically repeated parallel images. The basic repeat unit is called a supercell. How can we justify modeling the vapor phase as a vacuum? The point here is that the vacuum within the supercell does actually represent a vapor phase; however, the density of atoms in it is low. By regarding the supercell as a member of a grand canonical ensemble of systems at constant temperature and pressure, the chance of finding a gas molecule in such a small volume is indeed low, and does not significantly effect the internal thermodynamic variables E_s or G_s of the supercell. We mention that interfaces between crystals are treated in the same way as surfaces, except that a second crystal slab takes the place of the vacuum. We begin with the general thermodynamic formula for σ :

$$\sigma = \frac{1}{A_s} \left(G_s - \sum_i \mu_i N_i \right). \quad 1.$$

Here G_s denotes the total Gibbs free energy of the contents of the supercell, A_s is the surface area of the slab within the supercell, index i runs over all the component species: Ni, Al, and O; μ_i is the chemical potential of these species, and N_i is the number of atoms of each species contained within the supercell. We are assuming here for simplicity that the surfaces of the slab are identical. Recasting Equation (1) in terms of excesses Γ_i ,

$$\sigma = \frac{1}{A_s} \left(G_s - \frac{N_A}{N_A^b} G^b \right) - \sum_{i \neq A} \mu_i \Gamma_i. \quad 2.$$

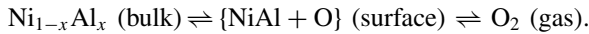
Here A represents the component with respect to which excesses are measured. This is possible at an interface with only one condensed phase; if there were two different condensed phases, two reference components would be required (42). N_A^b and G^b are the number of atoms of species A within an arbitrary representative quantity of the bulk phase and the Gibbs free energy of that quantity, respectively.

The surface excess Γ_i is given by

$$\Gamma_i = \frac{1}{A_s} \left(N_i - N_A \frac{v_i^b}{v_A^b} \right), \quad 3.$$

where v_i^b is the atomic fraction of component i in the bulk phase.

Now let us be more specific about the degrees of freedom under our control. We assume that the oxidized surface of the NiAl crystal (not necessarily stoichiometric) is in equilibrium with $\text{Ni}_{1-x}\text{Al}_x$ bulk and with oxygen gas at a certain partial pressure p_{O_2} . The equilibrium is



How many phases are there in the equilibrium? It would be incorrect to think about even several layers of the surface oxide as a separate phase, as the system does not have a well-defined bulk oxide region. Fortunately, it does not matter how thick the surface region of the oxidized metal is as long as there is some well-defined bulk metal. As there are $r = 2$ phases with $c = 3$ components (Ni, Al, and O) in equilibrium, one has $f = 3$ degrees of freedom according to the Gibbs phase rule:

$$f = c - r + 2 = 3 - 2 + 2 = 3.$$

Hence, p_{O_2} , T , and x can be chosen as three variables fully characterizing the system. We call them the environmental parameters because in a sense they provide an environment for the surface.

If, for example, Ni is chosen as the reference component, the above equations become

$$\sigma(x, T, p_{\text{O}_2}) = \frac{1}{A_s} \left(G_s - N_{\text{Ni}} \frac{g_{\text{NiAl}}(x, T)}{2(1-x)} \right) - \mu_{\text{Al}}(x, T) \Gamma_{\text{Al}} - \mu_{\text{O}}(p_{\text{O}_2}, T) \Gamma_{\text{O}}, \quad 4.$$

with the surface excesses of Al and O given by

$$\Gamma_{\text{Al}} = \frac{1}{A_s} \left(N_{\text{Al}} - N_{\text{Ni}} \frac{x}{1-x} \right), \quad \Gamma_{\text{O}} = \frac{1}{A_s} N_{\text{O}}, \quad 5.$$

and where g_{NiAl} is the Gibbs free energy of the bulk $\text{Ni}_{1-x}\text{Al}_x$ per formula unit:

$$g_{\text{NiAl}}(x, T) = 2 \{ (1-x) \mu_{\text{Ni}}(x, T) + x \mu_{\text{Al}}(x, T) \}. \quad 6.$$

Equations (4)–(6) are helpful for discussing which approximations need to be employed to make this a practical scheme. Recall that we intend to define a set of atomic configurations and stoichiometries of the supercell, calculate σ for each, and declare the one with the lowest σ to be our predicted equilibrium structure and corresponding surface energy. The most expensive part of the calculations is to obtain G_s because this involves the search for the atomic positions that

minimize the free energy of a slab containing from several tens to hundreds of atoms, and we want to use an ab initio method in order to properly account for the strength of chemical bonds. If G_s can be assumed to be independent of the three environmental parameters, it needs to be calculated only once for each member of the pre-selected set of atomic configurations. First of all, we assume that the effect of the pressure on G_s is negligible. In practice we set the external pressure to zero. Second, we consider the oxygen pressure to be low enough such that no oxygen atoms need to appear in the vacuum part of the supercell; and third, we assume that the concentration of oxygen atoms dissolved in the bulk is sufficiently small so that no oxygens need to be introduced explicitly into the interior of the slab. All these approximations are reasonable given that p_{O_2} will never exceed 1 atm. Similarly, one can neglect the dependence of G_s on x if the deviation of the alloy composition from the exact stoichiometry is of the order or less than $1/N$, where N is the number of metal atoms in the supercell. This condition places an upper limit on the range of compositions, which is important to keep in mind in dealing with compounds such as $Ni_{1-x}Al_x$, which exists as a homogenous phase in the range $0.40 < x < 0.55$. The most serious approximation is to neglect the temperature dependence of G_s . This dependence comes through both the vibrations of the atoms and the expansion of the lattice constant of the underlying bulk crystal. As such, it can be evaluated by means of explicit ab initio calculations; a number of studies of this type already exist (43–45). On the other hand, the variation of the chemical potential of oxygen with temperature is much stronger and thus dominates in the $\sigma(T)$ dependence. In other words, the assumption that G_s is just the zero-temperature total energy still gives reasonably accurate results. There is considerable cancellation of the bulk contributions to G_s with the second purely bulk term in the parenthesis of Equation (2).

In practical calculations then, the dependence of surface energy on x , p_{O_2} , and T in Equation (4) enters through the chemical potentials of the species, which, as the equilibrium condition is assumed, are equal to the respective chemical potentials in the bulk phases. As such, they can be calculated separately. With a few additional assumptions, their dependence on the environmental parameters can thus be estimated. In particular, for μ_O we can make use of accurate experimental data, so the main uncertainties are found in the chemical potentials of the species in the solid. This whole scheme is illustrated in Figure 1.

Chemical Potentials

SOLID PHASE Let us assume that the oxidized surface of NiAl is in chemical equilibrium with the underlying crystal so that the chemical potentials of Ni and Al, μ_{Ni} and μ_{Al} , are equal to those of the bulk phase. These chemical potentials depend on the composition x of the bulk phase $Ni_{1-x}Al_x$, as well as on temperature T and external pressure p . The pressure dependence of chemical potentials in solids can, of course, be neglected under normal conditions. Before proceeding with the discussion of how chemical potentials can be obtained in actual calculations, some

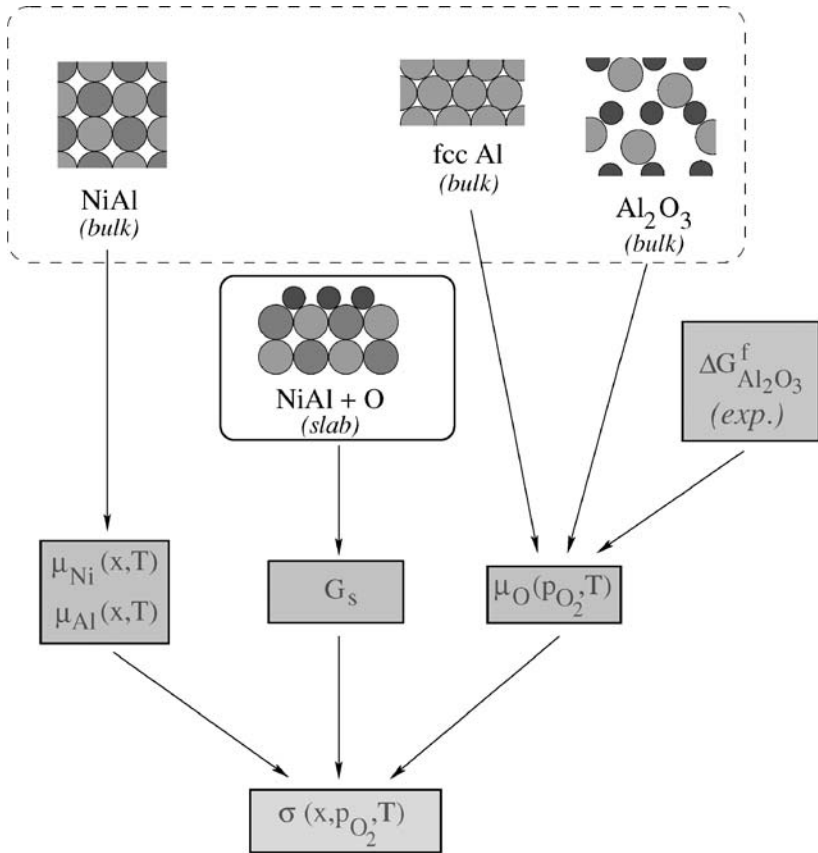


Figure 1 Schematic diagram describing the flow of data to obtain the surface energy σ as a function of the temperature T , partial pressure of oxygen gas p_{O_2} , and the composition x of the substrate $\text{Ni}_{1-x}\text{Al}_x$.

comment about their reference states is appropriate. It may be the case that chemical potentials used in semi-empirical calculations are not comparable with those used in ab initio calculations, and the latter in turn differ by orders of magnitude between all-electron and pseudopotential calculations. This is simply because in a semi-empirical calculation, isolated atoms (at rest) are taken to have a chemical potential of zero. On the other hand, in all-electron ab initio calculations, isolated nuclei and electrons may be assigned a zero value of chemical potential. In ab initio pseudopotential schemes the reference state would be isolated ions and valence electrons, and none of these corresponds to the chemical convention, which takes the enthalpy of an element at standard temperature and pressure as zero. Such dependence on the reference state should cancel out in the calculation of any physical observable such as σ , but it matters if data are transferred to one model

from another or from experiment. The chemical potentials of components in a solid may depend very sensitively on small concentrations of point defects. NiAl is a good example of this because it is a strongly ordered alloy, which if slightly Ni-rich, will support a population of Ni antisite defects (rather than Al vacancies). On the other hand if it is slightly Al-rich, this compound supports a population of Ni vacancies (rather than Al antisites). If we add one Al atom to an Al-rich alloy, it will create on average one more Ni vacancy, whereas if we add one Al atom to a Ni-rich alloy it will fill on average one Al vacancy. The energy required for the second process will be much less than for the first (at constant T). But this energy is precisely the chemical potential of Al in the alloy, which is therefore a sensitive function of stoichiometry near the stoichiometric composition. The chemical potentials in the case of NiAl have been estimated theoretically by the following procedure.

One assumes a dilute or ideal solution model, in which interactions between point defects can be neglected and they are randomly distributed. This is often referred to as the Wagner-Schottky model (46). Within this model, the Gibbs free energy $g(x, T)$ of a compound $A_{1-x}B_x$ is the sum of two kinds of terms. The first terms are linear in each defect and host atom concentration, and represent the point defect energies and vibrational entropies. The second terms describe the configurational entropy of the point defects. If only substitutional defects and vacancies are considered (which is a very reasonable approximation for NiAl), then the Gibbs free energy per formula unit is given by (47)

$$g(x, T) = \sum_{i,j} c_{ij} g_{ij}(x, T) + k_B T \sum_{i,j} c_{ij} \log c_{ij}, \quad 7.$$

where c_{ij} denotes the concentration (per sublattice site) of species I (A, B , or vacancy V) on sublattice J (A or B), g_{ij} are partial defect energies to be found from ab initio calculations, and k_B is Boltzmann's constant. Equilibrium concentrations c_{ij}^{eq} are those that minimize $g(x, T)$ given by (7), subject to some natural constraints: The sum of all the concentrations on each sublattice is unity, and the ratio of total concentrations of the A and B species is prescribed by the fixed composition x of the compound. If the defect parameters g_{ij} are known, the c_{ij}^{eq} can be obtained either by finding roots of a fourth-order polynomial (47) or by solving numerically the set of mass-action equations (48–50). Then the chemical potentials in question can be obtained directly. They are given by (47)

$$\mu_a = g_{aa} - g_{va} + k_B T \log \left(\frac{c_{aa}^{eq}}{c_{va}^{eq}} \right) \quad 8.$$

$$\mu_b = g_{bb} - g_{vb} + k_B T \log \left(\frac{c_{bb}^{eq}}{c_{vb}^{eq}} \right). \quad 9.$$

As $T \rightarrow 0$ K these chemical potentials as a function of x approach constants with a step at $x = 0.5$. The defect parameters g_{ij} can be assembled from total energy calculations for perfect supercells and for supercells containing a single defect, in

the approximation that the supercells are large enough for interactions between defects to be neglected. For example, if G_{va}^N is the Gibbs free energy of the supercell containing N unit cells with one vacancy on sublattice A , and g_0 is the free energy per unit cell of the ideal stoichiometric compound AB , then

$$g_{va}(T) - g_{aa}(T) = G_{va}^N(T) - Ng_0(T). \quad 10.$$

Note that the above Gibbs free energies might include the vibrations, but not the configurational entropy; the latter is already accounted for in Equation (7). Equations similar to Equation (10) can be obtained for all four types of point defects. Finally, we arbitrarily assign some value to g_{aa} and g_{bb} such that

$$g_{aa}(T) + g_{bb}(T) = g_0(T) \quad 11.$$

to complete the system of linear equations, which is sufficient to calculate all g_{ij} . It can be shown that arbitrary division of g_0 between g_{aa} and g_{bb} does not affect any physical properties of the system (47). In particular, μ_a and μ_b are well defined. If the supercell Gibbs free energies are approximated by zero-temperature total energies, the partial defect energies are also temperature independent.

So far, it has been demonstrated that the chemical potentials of a compound are unambiguously defined by the reference state chosen and by the energies of point defects. The alternative approach is to put natural bounds on the chemical potentials (51, 52) and to study a particular problem either over the whole range of chemical potentials specified by these bounds or simply for the maximum and minimum values of the allowed interval. In our case of the AB compound, this method works as follows. If μ_a , the chemical potential of component A , were to exceed that of the pure A crystal, μ_a^0 , component A would start to precipitate out of the compound. Hence

$$\mu_a \leq \mu_a^0; \quad \mu_b \leq \mu_b^0. \quad 12.$$

We also need the expression for the Gibbs energy g_0 of bulk alloy, which is given by Equation (6) for $\text{Ni}_{1-x}\text{Al}_x$, but which for the present purpose is sufficiently accurate if we take $x = 0.5$.

$$g_0 = \mu_a + \mu_b. \quad 13.$$

From Equations (12) and (13), one gets

$$\begin{cases} g_0 - \mu_b^0 \leq \mu_a \leq \mu_a^0, \\ \mu_b = g_0 - \mu_a \end{cases}, \quad 14.$$

in which only one of two chemical potentials is an independent variable. The above inequality is often recast in the equivalent form:

$$\Delta G_f \leq \Delta \mu_a \leq 0, \quad 15.$$

where $\Delta \mu_a = \mu_a - \mu_a^0$ and ΔG_f is the Gibbs free energy of formation of the compound AB . The method of bounds is often used in dealing with insulators or

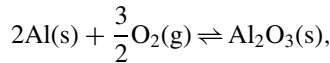
semiconductors where either the ab initio calculation of point defect statistics or the ideal solution model is more problematic than in metals.

GAS PHASE The last remaining ingredient needed in the expression for surface energy (4) is the chemical potential of oxygen $\mu_O(p_{O_2}, T)$. In fact, we need to know μ_O only for the standard pressure $p^0 = 1$ atm; one can then evaluate it accurately at any other pressure using the ideal gas expression:

$$\mu_O(p_{O_2}, T) = \mu_O^0(T) + \frac{1}{2}k_B T \log(p_{O_2}/p^0). \quad 16.$$

The superscript 0 on any quantity denotes its value at the standard pressure p^0 . Different authors have taken somewhat different approaches for calculating $\mu_O^0(T)$, but usually the information in research papers is insufficient for an uninitiated reader to follow the procedure with confidence. We therefore present our recommended approach in some detail.

The trick (34, 53) is to invoke a thermodynamic cycle corresponding to formation of some oxide, for which the standard Gibbs free energy of the oxide formation, $\Delta G_{\text{oxide}}^0(T)$, is available from tabulated experimental data. Here, we employ the reaction for $\alpha\text{-Al}_2\text{O}_3$ formation at standard partial oxygen pressure $p_{O_2} = p^0$:



in which $\text{Al}_2\text{O}_3(s)$ is the bulk crystal of $\alpha\text{-Al}_2\text{O}_3$, $\text{Al}(s)$ is the Al crystal, and $\text{O}_2(g)$ is oxygen gas. The Gibbs free energy balance for this reaction is

$$g_{\text{Al}_2\text{O}_3}^0(T) = 2\mu_{\text{Al}}^0(T) + 3\mu_{\text{O}}^0(T) + \Delta G_{\text{Al}_2\text{O}_3}^0(T). \quad 17.$$

Now we write our desired equation for $\mu_O^0(T)$ by turning this equation around, and we introduce an arbitrary reference temperature T_1 for reasons that will become clear:

$$\mu_O^0(T) = \frac{1}{3} \{g_{\text{Al}_2\text{O}_3}^0(T_1) - 2\mu_{\text{Al}}^0(T_1) - \Delta G_{\text{Al}_2\text{O}_3}^0(T_1)\} + \Delta\mu_O^0(T) \quad 18.$$

where

$$\Delta\mu_O^0(T) = \mu_O^0(T) - \mu_O^0(T_1). \quad 19.$$

The virtue of Equation (18) is that one does not have to calculate any absolute properties of an oxygen molecule directly; particularly, its internal energy at 0 K is subject to greater uncertainty than the energy of simple metals and their oxides, and one can now sidestep the problem of calculating it. The relative quantities $\Delta G_{\text{Al}_2\text{O}_3}^0(T_1)$ and $\Delta\mu_O^0(T)$ are readily obtained from tables of experimental data. Only the Gibbs free energy of bulk alumina per formula unit $g_{\text{Al}_2\text{O}_3}^0(T_1)$ and the Gibbs free energy per atom of a bulk fcc Al crystal $\mu_{\text{Al}}^0(T_1)$ must be calculated ab initio. These have been approximated by total energies at zero Kelvin. The lower

T_1 , the more accurate will be the result, but standard room temperature T^0 is adequate, which is fortunate because experimental values of $\Delta G_{\text{oxide}}^0$ are generally available only at and above T^0 . Notice that the value of $\mu_O^0(T)$ depends very much on the implicit reference states of the components in the ab initio calculation, which may be separated electrons and nuclei at rest (if all electrons are treated explicitly), or separated ions and nuclei at rest (in a pseudopotential calculation). However, this introduces no error because we are using the same convention for all the terms. Substitution of μ_O^0 back into Equation (16) completes the scheme:

$$\begin{aligned} \mu_O(p_{\text{O}_2}, T) = & \frac{1}{3} \{g_{\text{Al}_2\text{O}_3}^0 - 2\mu_{\text{Al}}^0 - \Delta G_{\text{Al}_2\text{O}_3}^0(T^0)\} \\ & + \Delta\mu_O^0(T) + \frac{1}{2}k_B T \log(p_{\text{O}_2}/p^0). \end{aligned} \quad 20.$$

One could choose any tabulated oxide instead of Al_2O_3 to close the thermodynamic cycle. The only requirement is that the chosen oxide and the oxide-forming element should be amenable to accurate first principles calculations. In theory, different oxides should lead to the same $\mu_O(T)$, but in practice there are small differences (41). Apart from experimental errors, the obvious reason for μ_O to differ from one oxide to another is the neglect of thermal contributions to the Gibbs energies of the solids, which are present in the experimental $\Delta G_{\text{oxide}}^0$. In principle this could be corrected by using the experimental data on the entropy and/or specific heat C_p of the bulk phases, if such information is at hand. Another source of error is intrinsic to density functional theory in which the errors in the treatment of exchange and correlation may differ from one system to another. Also, if pseudopotentials are used, they are not perfectly transferable.

Some observations on $\Delta\mu_O^0(T)$ are worth making. The best values of $\Delta\mu_O^0(T)$ are probably those based on combining experimental data with statistical mechanics for ideal gases (54). However, one could disregard experimental data and integrate from $\mu_O^0(T^0)$ to temperature T , using the formula for an ideal gas of rigid dumbbells (41):

$$\Delta\mu_O^0(T) = -\frac{1}{2} \{ (S_{\text{O}_2}^0 - C_p^0)(T - T^0) + C_p^0 T \ln(T/T^0) \}, \quad 21.$$

where $C_p^0(T) \equiv 7k_B/2$ and $S_{\text{O}_2}^0$ (the entropy of oxygen gas at $T = T^0$ and $p_{\text{O}_2} = p^0$) is the only parameter taken from thermodynamic tables. As seen in Figure 2, this simple formula, Equation (21), predicts the temperature dependence of $\Delta\mu_O^0$ surprisingly well; the error at 1000 K is only 0.005 eV rising to 0.036 eV at 2000 K.

Finally let us comment on the way ab initio data is used in Equation (20). So far we have assumed the 0 K total energies are estimates of the Gibbs free energies of solid phases (38). What if, instead, we take them to be estimates of the enthalpies (10). It has been suggested (27) that in condensed phases the enthalpy change Δh^0 between 0 K and T^0 is much smaller than the contribution to the Gibbs energy $T^0 s^0$, hence the second option is preferable. To clarify this point, we have compared the

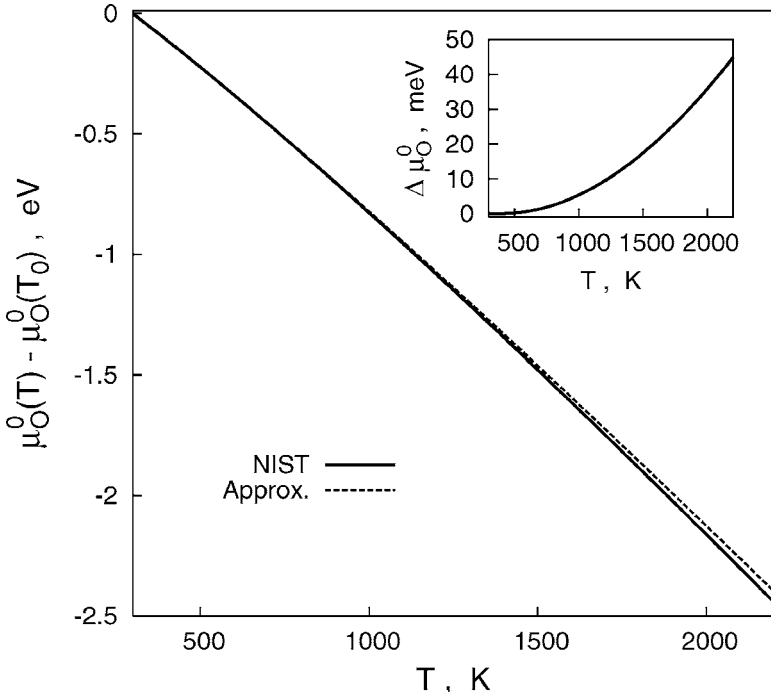


Figure 2 Chemical potential of oxygen μ_O^0 in the gas phase (per oxygen atom) relative to its value at $T_0 = 298.15$ K according to the NIST data (54) (*solid line*) and given by the approximate expression Equation (21) (*dashed line*). The difference between them is shown in the inset.

errors implied by either approach (see Table 1), using available experimental data. Although T^0s^0 indeed exceeds Δh^0 in most cases, these are of opposite sign. As a result, the differences $\Delta h^0 - T^0s^0$ are in many cases smaller in magnitude than Δh^0 . Although the errors listed in Table 1 are rather small, using the 0 K ab initio total energies as estimates of the Gibbs free energies is generally better than using them as estimates of the enthalpies.

Analytical Approximation

It is possible (although not strictly necessary) to make a further simplification of the calculations in order to explicitly reveal the main effects of the environmental parameters. One can approximate the composition dependence of chemical potentials (Equations 8–9) with simple algebraic expressions (47, 48) applicable in the range of concentrations near $x = 0.5$ over which the B2 phase is stable but still excluding a small region around the stoichiometric composition $x = 0.5$. The basic idea behind this approximation is to divide point defects present in an

TABLE 1 Comparison of the errors (in meV per oxygen atom) generated if one assumes that total energies at 0 K approximate either enthalpies (Method *H*) or Gibbs free energies (Method *G*) of crystalline oxide A_nO_m and oxide-forming element *A* in Equation (17). The errors are calculated as $[\Delta h_{A_nO_m}^0 - n\Delta h_A^0]/m$ (Method *H*) and $[\Delta h_{A_nO_m}^0 - n\Delta h_A^0 - T_0(s_{A_nO_m}^0 - ns_A^0)]/m$ (Method *G*), where $\Delta h^0 = h^0(T_0) - h^0(0\text{ K})$ is the enthalpy change and $s^0 = s^0(T_0)$ is the entropy change between 0 K and standard temperature $T_0 = 298.15\text{ K}$. The data are taken from References (54–57)

Oxide A_nO_m	$\Delta h_{A_nO_m}^0$, kJ/mol	Δh_A^0 , kJ/mol	$s_{A_nO_m}^0$, J/(mol K)	s_A^0 , J/(mol K)	Error, meV/at	
					Method <i>H</i>	Method <i>G</i>
Al ₂ O ₃	10.02	4.54	50.92	28.30	3.23	9.08
B ₂ O ₃	9.30	1.22	53.97	5.90	23.69	-19.73
BaO	9.98	6.91	72.05	62.48	31.83	2.27
BeO	2.84	1.95	13.77	9.50	9.19	-4.00
CaO	6.75	5.74	38.1	41.59	10.51	21.29
CdO	8.41	6.25	54.85	51.80	22.42	13.00
Cr ₂ O ₃	15.28	4.06	80.65	23.62	24.76	-9.64
GeO ₂	7.23	4.64	39.71	31.09	13.44	0.13
MgO	5.16	5.00	26.95	32.67	1.68	19.35
NbO ₂	9.27	5.26	54.50	36.46	20.81	-7.05
Nb ₂ O ₅	22.29	5.26	137.30	36.46	24.41	-15.35
SiO ₂	6.92	3.22	41.46	18.81	19.17	-15.81
SnO	8.74	6.32	57.17	51.18	25.01	6.51
SnO ₂	8.38	6.32	49.04	51.18	10.68	13.99
SrO	8.67	6.36	55.42	55.68	23.98	24.78
Ta ₂ O ₅	23.04	5.68	142.86	41.48	24.21	-12.80
TiO ₂	8.68	4.82	50.62	30.72	19.98	-10.75
ThO ₂	10.56	6.35	65.23	51.8	21.82	1.08
UO ₂	11.28	6.36	77.03	50.20	25.48	-15.96
UO ₃	14.59	6.36	96.11	50.20	28.40	-18.86
U ₃ O ₈	42.74	6.36	282.55	50.20	30.64	-20.31
VO	6.91	4.64	39.10	28.93	23.50	-7.91
V ₂ O ₃	17.48	4.64	98.16	28.93	28.32	-13.17
V ₂ O ₄	18.10	4.64	103.52	28.93	22.85	-12.41
V ₂ O ₅	21.51	4.64	130.40	28.93	25.34	-19.47
ZnO	6.93	5.66	43.65	41.63	13.22	6.99

ordered $A_{1-x}B_x$ compound into thermal and structural defects. The former are the result of thermal disorder; they disappear as $T \rightarrow 0$ K. The latter defects necessarily exist in the compound even at $T = 0$ K to maintain the given composition. The concentration of structural defects thus depends on the composition x but not on the temperature, and in a stoichiometric compound they are entirely absent. The ratio of thermal defects to structural defects is a small parameter, unless the composition is very close to stoichiometry; in real alloys the structural defects usually outnumber the thermal defects by orders of magnitude. The first term of a Taylor expansion of the chemical potentials with respect to this small ratio already turns out to be a good approximation. For NiAl in particular, there is good agreement with the exact formulae up to around 1400 K, as demonstrated in Reference (47) to which we refer the reader for more details. These expressions explicitly take into account that the constitutional defects in NiAl are Ni antisite atoms on the Ni-rich side and Ni vacancies on the Al-rich side, as found experimentally (58) and confirmed in a number of independent ab initio calculations (48, 49, 59, 60). Explicitly (47), on the Ni-rich side ($x < 0.5$):

$$\mu_a = \frac{1}{2} \{e_{aa} + e_{ab} + k_B T \log(1 - 2x)\}, \tag{22}$$

$$\mu_b = e_{bb} + \frac{1}{2} \{e_{aa} - e_{ab} - k_B T \log(1 - 2x)\}, \tag{23}$$

and on the Al-rich side ($x > 0.5$):

$$\mu_a = e_{aa} - e_{va} - k_B T \log \frac{2x - 1}{x}, \tag{24}$$

$$\mu_b = e_{bb} + e_{va} + k_B T \log \frac{2x - 1}{x}, \tag{25}$$

where a stands for Ni, b stands for Al, and x is the composition of the $Ni_{1-x}Al_x$ compound. In effect, Equations (22)–(25) approximate the dependence of chemical potentials on composition as being exclusively the result of the ideal configurational disorder of the structural defects on their own sublattices.

Another approximation used in Equations (22)–(25) is the neglect of terms of order $k_B T \delta$, compared with the $k_B T \log \delta$ terms, where $\delta = |x - 0.5|$ is the deviation of the composition of NiAl from the exact stoichiometry. We do not lose any essential physics in making this approximation, as the temperature dependence of surface energy σ is mainly from the oxygen chemical potential, even when compared with $k_B T \log \delta$ terms which we keep. To this order the formula for the surface energy Equation (4) simplifies to

$$\sigma(x, T, p_{O_2}) = \frac{1}{A_s} (G_s - N_{Ni} g_0) - \mu_{Al}(x, T) \Gamma'_{Al} - \mu_O(p_{O_2}, T) \Gamma_O, \tag{26}$$

where g_0 is the (free) energy of the unit cell of bulk stoichiometric NiAl, Equation (11), the aluminum surface excess is now the stoichiometry of the

supercell itself:

$$\Gamma'_{Al} = \frac{1}{A_s} (N_{Al} - N_{Ni}), \tag{27}$$

and $\Gamma_O = N_O/A_s$, as before. To make the surface energy dependence on all three environmental parameters explicit, we rewrite Equation (26) in the form

$$\begin{aligned} \sigma(x, T, p_{O_2}) = & \sigma_0 + \Delta\sigma_0\theta(x - 0.5) - \frac{1}{2}k_B T \{ \Gamma_O \log(p_{O_2}/p^0) \\ & + \Gamma'_{Al}\eta(x) \} - \Delta\mu_O^0(T)\Gamma_O, \end{aligned} \tag{28}$$

where σ_0 and $\Delta\sigma_0$ absorb all ab initio numbers, $\theta(x)$ is the step function and $\eta(x)$ is defined by

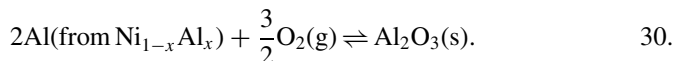
$$\eta(x) = \begin{cases} -\log(1 - 2x), & x < 0.5 \text{ (Ni-rich NiAl)} \\ 2\log[(2x - 1)/x], & x > 0.5 \text{ (Al-rich NiAl)} \end{cases} \tag{29}$$

and $\Delta\mu_O^0(T)$ can be parameterized as discussed above.

Stability Limits

Before we proceed with looking at the relative stability of various structures of a thin oxide film formed on the surface of NiAl, it is useful to estimate the range of stability of the respective bulk oxide phases. For example, if in the ab initio calculations we find a particular oxide layer to be stable at some p_{O_2} at which the NiAl substrate turns out to be unstable with respect to the formation of bulk Al_2O_3 , then the predicted surface structure is at best metastable with respect to further oxidation. It might still take much longer than the experimental timescale for the material to convert itself into a bulk oxide, e.g., because the oxide film itself is a barrier to further oxidation.

To find the p_{O_2} above which NiAl starts decomposing to form some bulk oxide phase, or equivalently, the pressure below which any bulk oxide would be unstable in contact with NiAl, we take the following approach. Imagine a system comprising a large sample of NiAl in contact with some bulk oxide surrounded by its vapor. The amount of the oxide phase is assumed to be large enough to consider it as a bulk phase and to neglect any surface or interface effects, but small in comparison to that of NiAl such that one could think of NiAl as a reservoir of Ni and Al atoms. We next check, in turn, three possible oxides to derive the p_{O_2} at which the equilibrium in the system is established at given temperature T and NiAl composition x and then choose the smallest of these pressures, p_{min} , as the p_{O_2} in question. This leaves us with only three representative situations to examine. The first one corresponds to NiAl releasing Al atoms to form Al_2O_3 :



The pressure p_a corresponding to the above equilibrium can be found as in (53):

$$\log[p_a(x, T)/p^0] = \frac{2}{3k_B T} [\Delta G_{Al_2O_3}^0(T) - 2\Delta G_{Al}(x, T)], \quad 31.$$

where ΔG_{Al} is the partial Gibbs free energy of Al atoms in NiAl. It can be taken from experiment (61), or calculated ab initio as $\Delta G_{Al}(x, T) = \mu_{Al}(x, T) - \mu_{Al}^0$. The values of p_a at 1273 K obtained in both ways are compared in Figure 3. The rather good agreement between them mirrors the similar level of consistency

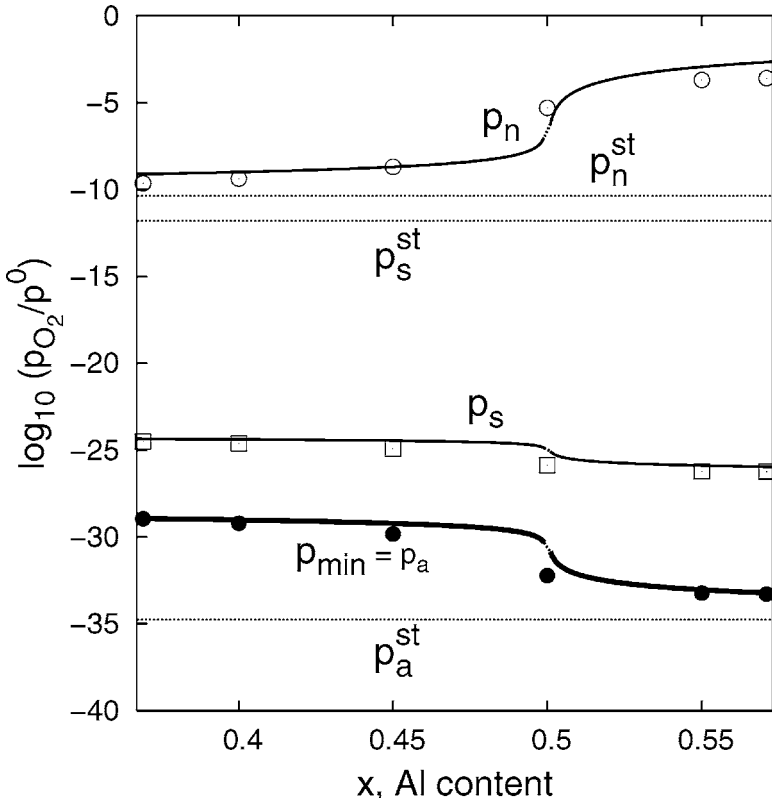
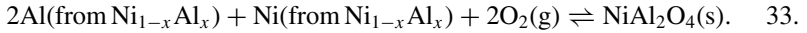
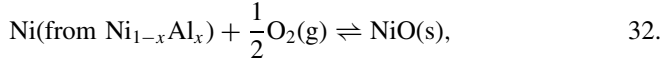


Figure 3 Composition dependence of p_a , Equation (31), p_n , Equation (34), and p_s , Equation (35) at $T = 1273$ K according to experiment (*symbols*) and ab initio calculations (*solid lines*) (62). The gaps on the curves in the vicinity of the stoichiometric composition appear because the analytical approximation for Ni and Al chemical potentials (Equations (22)–(25)), is not applicable there. Horizontal dotted lines indicate the boundary of the absolute stability of α - Al_2O_3 , p_a^{st} , Equation (37); NiO, p_n^{st} , Equation (38); and $NiAl_2O_4$, p_s^{st} , Equation (40). Experimental data are from Reference (23) ($\Delta G_{Al_2O_3}^0$ and ΔG_{NiO}^0), Reference (63) ($\Delta G_{NiAl_2O_4}^0$), and Reference (61) (ΔG_{Al} and ΔG_{Ni}).

between theoretical and experimental ΔG_{Al} explicitly shown in Reference (53).

The second and third reactions are similar to Equation (30) and describe the formation of nickel oxide NiO, and the spinel NiAl₂O₃, respectively:



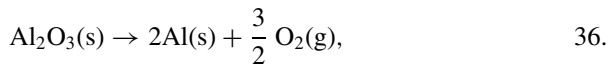
The pressures p_n and p_s corresponding to the equilibrium in Equations (32) and (33) are given by

$$\log[p_n(x, T)/p^0] = \frac{2}{k_B T} [\Delta G_{NiO}^0(T) - \Delta G_{Ni}(x, T)], \quad 34.$$

$$\begin{aligned} \log[p_s(x, T)/p^0] = \frac{1}{2k_B T} [\Delta G_{NiAl_2O_4}^0(T) \\ - 2\Delta G_{Al}(x, T) - \Delta G_{Ni}(x, T)]. \end{aligned} \quad 35.$$

These pressures are also plotted in Figure 3, which shows that p_a is lowest over the whole range of B2 compositions: $p_{min} = p_a$.

To complete our analysis, let us check that at the pressures found the respective oxides would not decompose into their constituents. The pressure p_a^{st} below which Al₂O₃ decomposes into Al(s) and oxygen gas



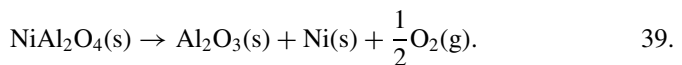
is defined by Equation (34):

$$\log[p_a^{st}(T)/p^0] = \frac{2}{3k_B T} \Delta G_{Al_2O_3}^0(T). \quad 37.$$

Similarly, NiO decomposes into Ni(fcc) and oxygen below pressure p_n^{st} given by

$$\log(p_n^{st}/p^0) = \frac{2}{k_B T} \Delta G_{NiO}^0(T). \quad 38.$$

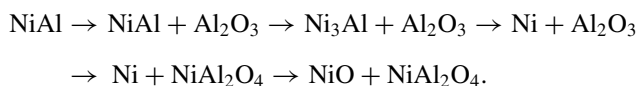
Finally, at an oxygen partial pressure below p_s^{st} , NiAl₂O₄ becomes unstable with respect to decomposition into Al₂O₃ and Ni (64):



where

$$\log[p_s^{st}(T)/p^0] = \frac{2}{k_B T} [\Delta G_{NiAl_2O_4}^0 - \Delta G_{Al_2O_3}^0]. \quad 40.$$

The pressures p_a^{st} , p_s^{st} and p_n^{st} are shown in Figure 3 as horizontal lines. Importantly, p_a^{st} is lower than p_a over the whole composition range (which simply means that it is harder to extract an Al atom from NiAl than from pure Al). Hence, the $p_a(x)$ curve represents the equilibrium between NiAl and alumina; above $p_a(x)$, NiAl starts shedding Al atoms to form Al_2O_3 . At $p_{\text{O}_2} = p_s$, NiAl might conceivably be in equilibrium with NiAl_2O_4 spinel, but because p_s is smaller than p_s^{st} , any NiAl_2O_4 formed should decompose into Ni and Al_2O_3 . We observe that increasing the p_{O_2} above p_a appears to activate more channels for NiAl oxidation. However, a mixture of products (including perhaps more metastable phases not considered here) is conceivable only if the local concentration of Al is depleted down to the Ni_3Al phase boundary and beyond by the slow bulk diffusion in the NiAl. Another way of looking at this is to consider the sequence of solid phases that would be in equilibrium under increasing p_{O_2} if the NiAl were completely exhausted, assuming it remains homogeneous. The sequence, both according to Figure 3 and the experimental phase diagram (65), would be



Note that NiAl_2O_4 *does* appear as a transient phase in some experimental studies of NiAl oxidation (66).

The pressure p_{min} is estimated here by assuming that bulk $\alpha\text{-Al}_2\text{O}_3$ is the oxide phase formed reversibly by NiAl. $\alpha\text{-Al}_2\text{O}_3$ is the most stable form of alumina, hence it is plausible to suggest that the pressure at which a thin oxide layer on top of NiAl starts to form could not be less than p_{min} . Clearly, a thin Al_2O_3 layer alone cannot be of lower energy than the bulk phase, otherwise the bulk α -alumina would decompose into such layers. However, one cannot rule out the theoretical possibility that the interaction of the layer with the substrate strongly stabilizes the system. This can be tested by ab initio calculations; so far the situation in which a thin oxide layer is more stable than bulk oxide has been found only for some noble and late transition metals: Ag (10), Ru (6), and Pd (13).

THE PATH OF NiAl OXIDATION

NiAl is a popular substrate for growing alumina films. It suits this purpose better than pure Al because the temperature required to convert the initially deposited oxygen atoms into an ordered film exceeds the melting temperature of Al. The experimental procedure to produce a 5 Å alumina film on NiAl(110) is well established (24). One must expose clean NiAl(110) to a dose 1000–1200 L (1 L = 10^{-6} Torr s) of oxygen at a temperature of about 600 K, after which the surface is annealed in ultra-high vacuum (UHV) at a temperature in excess of 1000 K. After the first stage, a layer of amorphous alumina is formed, which is believed to be locally ordered but which does not produce any diffraction spots (hence the name).

During the second stage, the well-ordered film of Al_2O_3 is formed. The question as to which of the allotropic modifications of Al_2O_3 most closely corresponds to the structure of the film is still being debated. Some experimental data suggest it is $\gamma\text{-Al}_2\text{O}_3$ (25, 67), although according to a very recent study (68), $\kappa\text{-Al}_2\text{O}_3$ reproduces experimental results even better. In either case, the structure of the film can be viewed as two distorted hexagonal layers of oxygens alternating with two aluminum layers, such that the film terminates with oxygen on the vacuum side.

Investigation into the influence of the above experimental conditions on the quality of the alumina film brings some surprising findings. It was shown that lowering the oxygen pressure from 5×10^{-7} Pa down to 5×10^{-8} Pa results in a better ordering of the film (69). This might indicate that the diffusion processes in NiAl are important, as the lower the pressure the longer the exposure time required to deposit the same amount of oxygen (1200 L) in (69). The effect of the temperature at the initial deposition stage is even more interesting: In going from 570 K to 670 K, the crystallinity of the film improves. A further rise in temperature to 720 K, however, makes the film worse again (70). The first observation apparently supports the previous diffusion argument, whereas for the second the authors of (70) find no reasonable explanation. Also puzzling remains the observation that after the initial deposition performed at relatively low-temperature 370 K, even subsequent high-temperature UHV annealing does not produce the expected form of the oxide film (71).

To rationalize the results of such experiments, or even to give some guidance for future experimental work, a model of surface oxidation of NiAl at the atomistic level would be helpful. More generally, oxidation of a perfectly ordered compound in which only one of the components participates in the formation of the oxide film, sometimes referred to as selective oxidation, is not unusual. Elucidating the main rules governing the much-studied NiAl may help to understand the oxidation of other compounds, such as CoAl (72) and CoGa (Ga_2O_3 film) (73). What is known about the mechanism of NiAl oxidation? Evidently oxygen should somehow initiate the segregation of aluminum to the surface, where aluminum oxidizes. In the later stages of oxidation, i.e., after the formation of a continuous oxide layer, its further growth occurs by means of diffusion of Al and O atoms through the film in opposite directions. Parabolic kinetics of the growth of the thick oxide indicates that the process is diffusion controlled (1). For the early stage at which a thin film just forms, Al segregation to the surface might proceed by more than one mechanism. Bulk $\text{Ni}_{1-x}\text{Al}_x$ with Al in excess ($x > 0.5$) forms a subtractional solid solution, in which extra Al atoms stay on their own sublattice thus creating vacancies on corresponding Ni sites (see above). If this is still the case close to oxidized surfaces, segregation of Al would effectively mean segregation of V_{Ni} . Otherwise Al_{Ni} atoms should appear at the interface. Such antisite Al defects do not usually appear in NiAl bulk, except in very Al-rich alloys (47, 49). Nevertheless, NiAl actually uses both mechanisms (see below).

A related question is whether the extraction of Al atoms from the NiAl crystal during oxidation increases the vacancy concentration in the specimen, as Frazer

et al. (74) suggested to explain the growth of voids and dislocation loops in a slowly cooled NiAl crystal that they observed during annealing in 10^{-7} Torr vacuum at about 1200 K. Although Eibner et al. (75) noted that Fraser et al.'s result could be interpreted without any assumption of vacancy injection by surface oxidation, the later experiment by Parthasarathi & Fraser (76) seemed to support the initial idea. Jaeger et al. (24) suggested that the formation of the Al_2O_3 film should destroy two surface layers of NiAl with subsequent dissolution of Ni atoms into the bulk, the latter being the reason for the ordering of the Al_2O_3 overlayer during annealing at high temperature. In this case, there should be vacancy consumption rather than vacancy injection into the bulk. Our analysis supports the view that vacancies are consumed rather than created during the initial stage of the oxidation.

ZERO TEMPERATURE CALCULATIONS: THE ROLE OF POINT DEFECTS It is apparent from the above discussion that the creation and annihilation of point defects in the surface region of NiAl is an essential part of the process. To elucidate a plausible mechanism for the oxidation we therefore considered a number of different scenarios, introducing into the NiAl substrate either vacancies or antisite defects, or both. The simulation cell used in our ab initio calculations consisted of four layers with two Ni and two Al atoms in each layer. Zero, one, and three O atoms were added to the cell; the latter imitates a complete Al + O layer of the oxide film, half of what is observed experimentally, whereas configurations with one oxygen atom per cell were supposed to model single atom adsorption. For completeness, we also considered configurations with two Al + O layers, with six oxygen atoms per simulation cell. We denote the configurations with a capital letter and a subscript. The meaning of the former is given in Table 2 in which all the configurations are listed. The subscript indicates how many O atoms were introduced in the supercell, which at the same time is the oxygen excess times the surface area, $\Gamma'_O A_s$. For example, A_0 denotes the clean ideal NiAl surface, E_3 is the configuration with 3 oxygen atoms per 4 surface sites of the substrate, the latter contains a vacancy on the Ni sublattice in the top layer, $V_{\text{Ni}}^{(1)}$, in addition a Ni atom in the top layer and an Al atom in the second layer are interchanged, $\text{Al}_{\text{Ni}}^{(1)} + \text{Ni}_{\text{Al}}^{(2)}$ (the so-called exchange defect).

In each of the configurations, the atomic positions were adjusted to minimize the energy of the slab. For oxygen-free configurations this was straightforward. In configurations containing one O atom, we placed it on inequivalent adsorption sites (40) and then compared the respective total energies after atomic relaxation. For three and more oxygen atoms we adopted the following strategy: First, a particular configuration was brought to the nearest (local) minimum, and then we performed a molecular dynamics simulation at $T = 1000$ K monitoring the potential energy of the system. After 300–500 MD steps we took the lowest point on the potential energy surface as a starting point for the final zero-temperature optimization of atomic positions. The advantage of the MD method is that it probes collective

TABLE 2 Notation for different configurations considered in the present study. Point defects are denoted as $X_Y^{(i)}$, which means species X (Al, Ni, or vacancy V) on sublattice Y (Al or Ni) in layer i (layer 1 is the surface). Configuration H was designed to simulate experimentally observed stoichiometry of the oxide (two Al_2O_3 layers); it was used in combination with 6 oxygen atoms (H_6 in our notation). The last column represents the surface excess of Al atoms Γ_{Al} (assuming a stoichiometric substrate) multiplied by the cross-sectional area of the supercell A_s

Notation	Point defects present	$\Gamma_{\text{Al}} \times A_s$
A	none	0
B	$V_{\text{Ni}}^{(2)}$	1
C	$V_{\text{Ni}}^{(1)}$	1
D	$V_{\text{Ni}}^{(2)} + \text{Ni}_{\text{Al}}^{(2)} + \text{Al}_{\text{Ni}}^{(1)}$	1
E	$V_{\text{Ni}}^{(1)} + \text{Ni}_{\text{Al}}^{(2)} + \text{Al}_{\text{Ni}}^{(1)}$	1
F	$V_{\text{Al}}^{(2)} + \text{Al}_{\text{Ni}}^{(1)}$	1
G	$\text{Ni}_{\text{Al}}^{(2)} + \text{Al}_{\text{Ni}}^{(1)}$	0
H	$V_{\text{Ni}}^{(1)} + \text{Ni}_{\text{Al}}^{(2)} + \text{Al}_{\text{Ni}}^{(1)} + \text{Al extra atom}$	2
I	$V_{\text{Al}}^{(1)}$	-1
J	$V_{\text{Ni}}^{(1)} + \text{Ni}_{\text{Al}}^{(1)}$	-1

motions of the atoms and can be good at finding natural pathways linking different basins of the potential energy surface. As a result, we managed to locate new configurations that would be impossible to guess otherwise. In some cases, these configurations were 1–2 eV/cell lower in energy than those obtained from initial plausible atomic arrangements. For more details and discussion of the MD simulations and all ab initio calculations, which were made with the plane-wave pseudopotential method using the CPMD code, the reader is referred to References (40, 53). Below we present only the results obtained within the local density approximation (LDA). The effect of the generalized gradient approximation (GGA) is discussed in (40).

The study of the adsorption of one O atom per supercell, $\Gamma_{\text{O}} A_s = 1$, reveals that oxygen atoms prefer to adsorb at the threefold hollow site formed by two Al and one Ni atoms. The second oxygen's preference is the bridge site between Al atoms, which is just 0.2 eV higher in energy. Strong distortion of the substrate was observed in both cases. According to structural models of the $\text{NiAl}(110)/\text{Al}_2\text{O}_3$ interface (24, 25), configurations with $\Gamma_{\text{O}} A_s = 3$ should correspond to one of the two Al + O bilayers of the Al_2O_3 . However, the theoretical structure of the oxygen layer on the *ideal* NiAl substrate does not at all resemble any atomic arrangement typical of Al_2O_3 . O atoms have arranged themselves there in a kind of butterfly structure, occupying an Al–Al bridge site and two (2Al + Ni) hollow sites per

cell (configuration A_3 in Figure 4), providing each O atom with two Al neighbors. However, it is problematic to call such a structure an oxide layer because the parallel O–Al chains do not appear to be linked to each other. Configuration G_3 , in which we exchanged a surface Ni with subsurface Al atoms, would not seem particularly stable either (see Figure 4). Owing to its larger radius, the extra Al atom has been pushed out of the surface and forms a kind of pyramid with its four nearest-neighbor Al atoms. This pyramid is decorated with oxygens on three of its four sides in such a way that each O atom now has three Al neighbors. Nevertheless, the total energy of this structure is almost 2 eV lower, probably because of the increased number of O–Al bonds.

We checked next the effect of introducing a Ni vacancy in the top layer (configuration C_3). The energy again significantly decreased (by 1.92 eV for Ni-rich, and by 2.96 eV for Al-rich NiAl). During the MD run, atoms first vibrated about their initial positions, but after about 300 steps (0.36 ps) the Al atoms changed their striped structure by forming distorted hexagonal rings around Ni atoms, in which each pair of adjacent Al atoms became connected by an oxygen atom. Although each oxygen atom in this structure still had only two Al neighbors, the extra space provided by the vacancy allowed the system to form a number of short O–Al bonds (1.79 Å). We thus conclude that the effect of an antisite defect is to expose more Al atoms to the surface oxygen and thus to increase the number of Al–O bonds, whereas the vacancy makes space for the system to arrange atoms in a more optimal way.

Finally, trying both the exchange defect and the Ni vacancy in the top layer simultaneously, we arrived at our lowest energy atomic arrangement, which demonstrates two clearly separated oxygen and aluminum layers (configuration E_3 in Figure 4). Al atoms in the top layer arrange themselves in a distorted hexagonal packing and have almost lost their sublattice individuality, therefore the resulting O–Al bilayer can be considered as the first distinct precursor of the oxide phase.

How does the system arrive at the configuration E_3 starting from configuration A_3 ? Would it go through G_3 or C_3 (Figure 4)? To answer this, we have considered a number of intermediate configurations listed in Table 2, such that the system's trip from A_3 to E_3 can be decomposed into elementary steps. The resulting pathways are shown in Figure 5 together with the energy change at each step. For example, if a Ni bulk vacancy is initially absorbed by the second layer ($A \rightarrow B$), it may then jump to the surface layer ($B \rightarrow C$), and the creation of exchange defect ($C \rightarrow E$) completes the path $ABCE$. Alternatively, having a Ni vacancy in the second layer, the system can first create an exchange defect ($B \rightarrow D$) and then either allow the Ni vacancy to jump to the first layer immediately ($D \rightarrow E$), or first convert $V_{Ni}^{(2)}$ and $Ni_{Al}^{(2)}$ defects into $V_{Al}^{(2)}$ (i.e., the Ni antisite atom returns to its own sublattice, filling a Ni vacancy there). A nearest-neighbor Ni atom from the first layer can then jump into this vacancy ($D \rightarrow F \rightarrow E$). Another family of pathways arises if we assume that the system starts by creating an exchange defect ($A \rightarrow G$). Then a Ni vacancy arrives at the second layer ($G \rightarrow D$), and the subsequent history is as above.

We emphasize here the dependence of the relative energies on the substrate composition. In the zero-temperature limit, the surface energy dependence on composition is described by the step function, Equation (28). Hence the precise composition of the bulk substrate is not important, only whether it is Al- or Ni-rich. Looking at the pathways shown in Figure 5 we see that an additional free-energy barrier of at least 0.5 eV appears on the Ni-rich side compared with that on the Al-rich side (40). This is because configurations containing a Ni vacancy are higher in energy in Ni-rich NiAl simply because on the Al-rich side, these vacancies are the structural defects (see above).

Our zero-temperature analysis thus shows that the oxidized NiAl substrate tries to get rid of Ni atoms in the top layer(s) by either exchanging them with Al atoms beneath or absorbing Ni vacancies from the bulk. Both processes seem essential: The first allows the surface to expose more Al atoms to oxygen, whereas the second provides more space in the surface layer to accommodate larger Al atoms and subsequently to form a relatively open oxide structure (77). On the Ni-rich side, we expect larger barriers for the oxidation. For any substrate composition, the initial growth of the oxide film invokes the segregation and further consumption of Ni vacancies, therefore the substrate vacancies are destroyed, not injected.

This picture remains essentially valid in the finite temperature analysis (see below). Before proceeding, however, let us discuss how realistic the suggested mechanism is. In particular, according to the presented scheme one would expect that the substrate is first locally enriched with Ni near the metal-oxide interface, and this has not been observed experimentally (25). Of course, such enrichment is a transient effect; the excess Ni atoms should dissolve in the bulk to restore the overall equilibrium of the system by absorbing Ni vacancies. But is the diffusion in bulk NiAl fast enough to supply all the required vacancies?

To confirm that this is the case, one could make a routine estimate of the diffusion rates (24, 69), but we think more direct evidence exists. It comes from the elegant work by McCarty et al. (78), who observed the growth and shrinkage of surface steps at the NiAl(110) surface while cycling the temperature around 1000 K. The characteristic time of the cycle was of the order of several seconds. This turned out to be sufficient for the surface steps to respond to the temperature oscillation by changing their size. The essential point is that the size of the steps changed because they were emitting or absorbing vacancies to maintain the temperature-dependent equilibrium concentration of vacancies in the NiAl bulk.

Even more direct confirmation of the model comes from the X-ray study of the NiAl(110)/Al₂O₃ interface by Stierle et al. (71). The exposure of the NiAl specimen to oxygen gas at two different temperatures, 370 K and 570 K, followed by a 4 min annealing at 1020 K, resulted in drastically different concentrations of point defects in the first few layers of the substrate. At the lower exposure temperature, almost half of the aluminum sublattice was occupied by vacancies in the first two layers. In addition, the Ni sublattice of the top layer contained Ni and Al atoms in almost equal proportion. We understand that the temperature

of 370 K was insufficient to activate the diffusion, and the oxidation removed a significant fraction of the Al atoms from the substrate leaving Al vacancies; the very open structure that resulted induced major chemical disorder on the sublattices. Some structural disorder is to be expected in such open structures, especially in the vicinity of the incommensurate oxide phase. At the higher temperature, $T = 570$ K, on the contrary, no vacancies were found in the top two layers, and only 18% of Al antisite atoms was observed. These atoms were significantly displaced outwards (by half of the NiAl(110) interplanar spacing). We consider the above result as evidence of some diffusion exchange already in operation at 570 K. The antisite Al atoms are probably the consequence of the strong chemical interaction between the oxide layer and the NiAl substrate. Surprisingly, introduction of 11% of Ni atoms in a Ni-Ni bridge site in the surface layer led to significant improvement of the fit to X-ray data (71). This might be a consequence of the above mentioned lateral distortion of the substrate atoms induced by the oxide film. Somewhat different results have been reported by Torrelles (79). In this study (1200 L at 600 K, then annealing to 1200 K for few minutes), neither structural nor additional chemical disorder in the top substrate layer was detected after the formation of the Al₂O₃ overlayer. The intermixing of the species between sublattices in the top layer of about 4% was the same as for the pure NiAl(110) surface. Such results are interpreted in (79) as the result of the diffusion of Al to the surface and Ni to the bulk.

Overall, we conclude that the point defect-mediated oxidation mechanism (40, 53), controlled by defect mobility as a function of temperature, is fairly well documented in NiAl. The rate of diffusion required for this mechanism is already noticeable at temperatures of about 600 K, and is surely sufficient at 1000–1200 K.

Surface Energy Dependence on the Environmental Parameters

In this section, we expand the analysis made above to finite temperatures. In doing this, we neglect any vibrational contributions to the Gibbs free energy, thus simply converting each of the previously calculated zero-temperature surface energies into a function of p_{O_2} , x , and T by using Equation (28). We concentrate on the following two issues: What is the lowest energy configuration at a given set of environmental parameters? Do any oxidation barriers appear in addition to those previously discussed? Notice in the following that a classical treatment of surface energies would distinguish the surface of the film from its interface with the substrate, and attribute a separate interface energy to the latter. We recognize that this distinction has no meaning when the films are too thin for their surface to be decoupled from the interface with the substrate, and we note that our surface energies include this coupling implicitly, together with the surface and interface contributions.

We plot in Figure 6 the surface energies σ of our configurations as a function of p_{O_2} at $T = 1273$ K, separately for a Ni-rich ($x = 0.45$) and an Al-rich ($x = 0.55$) composition. In this way we can determine the behavior of σ at all intermediate

compositions, as it should change smoothly from Figure 6a to Figure 6b as x goes from 0.45 to 0.55. The observation widely used in similar studies [(see, for example, References (26, 29)] is that changing the temperature roughly corresponds to rescaling the pressure axis if the latter is plotted in units of $\log(p_{\text{O}_2}/p^0)$ (34). This is because the composition-dependent term is small compared with the oxygen pressure term in curly brackets in Equation (28). The last term in Equation (28) defines the pressure about which the rescaling should be performed. For NiAl, this is a large pressure of about 10^{11} atm (53). Therefore, all essential information is already contained in Figure 6.

In Figure 6 we show only configurations A , C , E , and H as this is sufficient to capture the overall picture. Different configurations are shown by different colors, whereas the oxygen excess $\Gamma_{\text{O}A_s} = 1, 3, \text{ or } 6$, is indicated by numbers on the plot. Horizontal lines correspond to zero oxygen excess, meaning an oxygen-free surface. Let us start with the Ni-rich system (Figure 6a). The structure of this busy plot is in fact quite simple. One can distinguish three regions indicated above the plot. Region I corresponds to the pressures at which the clean surface (A_0) is most stable. These are the pressures below $\sim 10^{-24}$ atm. Region III is the region in which the oxidation can proceed without any additional barriers. It corresponds to the pressures above $\sim 10^{-14}$ atm. Indeed, it is easy to appreciate that the following sequence decreases the surface energy at each step: $A_0 \rightarrow A_1$ (an O atom adsorbs at the clean surface), $A_1 \rightarrow A_3$ (two more O atoms adsorb), $A_3 \rightarrow C_3$ (a Ni vacancy arrives at the top layer), $C_3 \rightarrow E_3$ (an exchange defect is created), $E_3 \rightarrow E_6$ (three more O atoms adsorb), and $E_6 \rightarrow H_6$ (an Al atom is extracted from the substrate).

Correspondingly, Region II is the region in which an additional barrier for the oxidation appears owing to the non-monotonic dependence of surface energies on oxygen coverage. This situation arises if, for example, configurations with three oxygen atoms per cell are lower in energy than configurations with one oxygen atom, but clearly the surface cannot adsorb three atoms before it adsorbs one! This behavior is discussed below. The paths that the system can choose in such circumstances are $A_0A_1C_1C_3E_3E_6H_6$ or $A_0C_0C_1C_3E_3E_6H_6$ (Figure 6a).

If we look only at the lines representing the lowest σ , these are A_0 below the pressure 10^{-24} atm, and H_6 above it. Therefore, there is a range of pressures between p_{min} and 10^{-24} atm. in which the substrate should already be oxidizing (see above), but this does not happen according to the calculations of surface energy. There might be two reasons for this. First, the estimate refers to the formation of bulk $\alpha\text{-Al}_2\text{O}_3$ by oxidation of NiAl, and the thin oxide film that forms on the surface may be less stable than bulk alumina. Second, in calculations, we can consider only a limited number of configurations; there might be a configuration of lower energy than H_6 , which would intersect A_0 at a lower pressure. The low-energy configurations for each coverage for which calculations are available (A_0 , A_1 , E_3 , and H_6) form a sequence in which configurations with progressively higher oxygen content intersect A_0 at lower and lower pressure. They should tend to a vertical line in the limit of infinite oxygen excess (a thick Al_2O_3 layer). Without extrapolating from the present configurations, we note that at a pressure of $\sim 10^{-21}$ atm, the H_6

line intersects the zero axis, which signals the instability of the system to catastrophic oxidation. We interpret $\sigma < 0$ to mean that the whole system is unstable to fragmentation into oxidized surfaces.

For the Al-rich substrate (Figure 6b), the situation is similar, except the vacancy-containing configurations (C , E , and H) are of lower energies because they have Al in excess. As a result, the boundaries for Regions I, II, and III shift slightly to the left: 10^{-26} and 10^{-16} atm instead of 10^{-24} and 10^{-14} atm, respectively. Also, the nominal barriers for paths $A_0A_1C_1C_3E_3E_6H_6$ and $A_0C_0C_1C_3E_3E_6H_6$ in Region II are lowered on the Al-rich side. This is the same trend we observed for transitions at fixed oxygen coverage (see above).

According to Figure 6, the experimental conditions under which the oxide film on NiAl is grown (for the initial oxygen deposition and even for the high-temperature annealing) fall into Region III for both Ni-rich and Al-rich substrate. Although the metal is already unstable with respect to oxidation (configuration H_6 gives a negative surface energy), surprisingly, a thin oxide film can still be produced. This is likely due to kinetic limitations: The diffusion of oxygen and/or aluminum through the compact oxide film is sufficiently slow to prevent its further growing. However, it remains unclear how to explain the following experimental observation: If the annealing temperature exceeds 1300 K, the oxide film starts to disintegrate (80). According to Figure 6, in order for the oxide film to dissolve at 1300 K, the p_{O_2} must be of the order of 10^{-24} atm or even lower. We can only speculate that lower values than this might prevail at the oxide-metal interface if the diffusion gradient is sufficiently steep.

'Inverted' Surface Energy Behavior and Relation to the Oxide Growth Mode

Previously, we pointed out a surprising feature of $\sigma(p_{O_2})$ lines as the p_{O_2} is raised: At the point where a configuration with oxygen excess $\Gamma_O A_s = 1$ becomes stable, i.e., crosses the clean surface line A_0 , a configuration with $\Gamma_O A_s = 3$ is already more stable. We call this behavior inverted. Similarly, when $\Gamma_O A_s = 3$ becomes more stable than A_0 , a $\Gamma_O A_s = 6$ configuration is already more stable. This is opposite to the picture that one would naively expect, thinking of adsorbed oxygen atoms as negatively charged ions that repel each other. Indeed, a monotonic decrease of binding energy per adatom as the coverage increases is often observed for other systems such as O/Ru(0001) and O/Rh(111) (6, 7), up to a monolayer coverage. A normal pattern would correspond to $\sigma(p_{O_2})$ plots shown on the left graph in Figure 7, in which the lines with higher oxygen content intersect the pure surface line at higher pressures. For NiAl(110), the situation is reversed, and this inverted behavior is shown on the right graph in Figure 7. Why do surface energies of oxidized NiAl show this counterintuitive trend? The answer is rather simple, but before we explain it, let us make one more observation. The lowest energy configurations for each oxygen coverage, A_0 , A_1 , E_3 , and H_6 on the Ni-rich side, and A_0 , C_1 , E_3 , and H_6 on the Al-rich side, both form the inverted sequence (Figure 6).

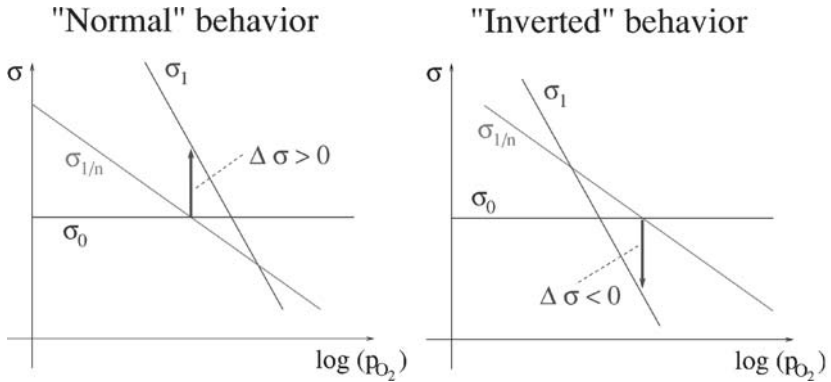


Figure 7 Schematic illustration of the normal and inverted dependence of surface energy on coverage. In this example, we show surface energies corresponding to coverages 0 ML, 1 ML, and some fractional coverage of $1/n$ ML, where $n > 1$. The normal type corresponds to σ_1 crossing σ_0 at higher oxygen partial pressure than $\sigma_{1/n}$; the type is inverted if this is the other way round. The normal (inverted) type is indicated by the positive (negative) sign of $\Delta\sigma$ defined by Equation (42) and has a simple geometric interpretation, as shown in the Figure.

However, by comparing only A_i configurations in which no point defects are allowed (Figure 6), we see that they form a normal sequence. Hence, it is the point defects created in the substrate that invert the surface energies. Now the picture we have is thus. Because of the strong attraction between adsorbed oxygen atoms and substrate Al atoms, the adsorbate tries to re-arrange the substrate to create the local configuration that would resemble stable alumina as closely as possible. Apart from simple atomic relaxation (which is also present in configurations A_i), such a rearrangement requires absorption of vacancies and interchange of Al and Ni atoms. If these movements can be achieved, the more oxygen atoms that combine forces, the lower the energy of the structure they create. The gain in energy overcomes the above mentioned mutual repulsion and the disadvantage of sharing substrate atoms. In other words, if point defects are available, the oxygen atoms can work together to design the substrate that suits them best. If point defects are not available, then the ability of the adsorbed oxygens to cooperate is reduced.

There is a direct relation between inverted versus normal behavior of the surface energies and the the stability of islands versus a continuous film, illustrated in Figure 8. Consider two configurations with surface energies σ_m and σ_n , where the subscript is an integer that measures the oxygen excess Γ_O , and $m < n$. The monolayer corresponds to $n = 1$, the double layer to $n = 2$ and so on. σ_0 denotes the energy of the pure surface. The islands in Figure 8 contain the same material as the continuous layer, but have a relative thickness n/m . They therefore occupy a fraction m/n of the surface and the combination of exposed surface and islands

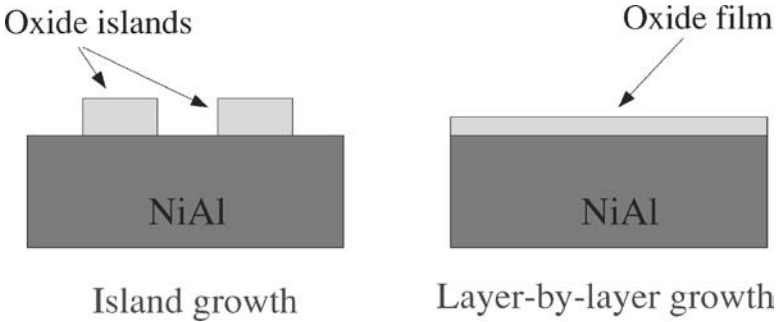


Figure 8 Illustration of the island growth and layer-by-layer growth modes of the surface oxide.

has an effective surface energy of

$$\sigma_{islands} = \frac{m}{n}\sigma_n + \left(1 - \frac{m}{n}\right)\sigma_0. \tag{41}$$

Compare this with the surface energy σ_{layer} of the continuous layer on the right of Figure 8 and define

$$\begin{aligned} \Delta\sigma(x, T) = \sigma_{islands} - \sigma_{layer} = m \times & \left\{ \frac{1}{n}\sigma_n(x, T, p_{O_2}) \right. \\ & \left. + \left(\frac{1}{m} - \frac{1}{n}\right)\sigma_0(x, T) - \frac{1}{m}\sigma_m(x, T, p_{O_2}) \right\}. \end{aligned} \tag{42}$$

All surface energies depend on three environmental parameters, except for σ_0 , which does not depend on p_{O_2} . However, the dependence of σ_n/n and σ_m/m on p_{O_2} cancels out in Equation (42). Therefore, $\Delta\sigma$ does not depend on p_{O_2} , which we explicitly indicate in Equation (42). Now it is easy to see that the normal (inverted) regime corresponds to positive (negative) $\Delta\sigma$: one just needs to substitute into Equation (42) the pressure at which $\sigma_m = \sigma_0$. The theory we have just presented is a discrete version of a phenomenon known in the theory of adsorption, namely that if the surface energy as a function of coverage is convex, it is favorable for the adsorbate to partition into areas or phases of unequal coverage, and conversely. Our set of inclined lines of surface energy versus p_{O_2} are sampled from a much larger set of such lines, from which, in principle, a continuous curve of surface energy versus coverage could be constructed. That this curve would be convex can be seen by noting just the three lines drawn in the right hand graph of Figure 7.

Of course, there should be some additional penalty owing to the boundaries of the islands. This affects the minimum size of the islands beyond which such a phase separation lowers the surface energy. We conclude that the inverted behavior, which is demonstrated by the calculated surface energies of oxidized NiAl, should favor the oxide initially appearing as isolated islands, and not the layer-by-layer

growth mode (Figure 8). The layer-by-layer mode would, however, be energetically favored if the supply of point defects from the substrate were suppressed, such as by lowering the temperature.

The above conjectures have some experimental support, although it is probably not conclusive. Recall here that the fabrication of the oxide layer on NiAl(110) is a two-step process (see above): 1200 L of oxygen is initially deposited at about 600 K, which results in a layer of amorphous alumina (α -Al₂O₃) covering the whole surface. In a second step, high-temperature annealing leads to the formation of well-ordered crystalline Al₂O₃ on top of NiAl. During the first step, the bright diffraction spots caused by the substrate gradually disappear, and no diffraction pattern is observed by the end of the process. No oxide islands are observed at this stage (80). In the second step, holes revealing clean surface re-appear (80), as the ordered crystalline alumina is more compact than α -Al₂O₃. Hence, another cycle of oxidation is required to fill these holes (81). The formation of the patches of clean surface is more likely related to the crystallization of the α -Al₂O₃ than to the growth mode, but the driving force would be the same. Direct observation of the growth of an ordered alumina film on an otherwise clean NiAl(110) would resolve this question. Perhaps, the most relevant observation is that of McCarty (80), who initially exposed a Ni₅₇Al₄₃ sample to a low dose of oxygen (360 L) at 325°C, after which low-energy electron microscopy (LEEM) micrographs showed that the oxygen adsorbed uniformly. After annealing at 925°C, most of the substrate became oxide free, with relatively few oxide islands being formed at terraces and step edges. (Interestingly, some of these oxide patches were of a type different from those produced by the standard procedure, an observation similar to that in Reference (71)). Thus McCarty's results suggest that the high-temperature, ordered Al₂O₃ does prefer to form islands rather than to spread itself over the surface, and that a transition between these two types of behavior should occur somewhere between 600 K and 1200 K. According to our interpretation, the transition temperature is the temperature at which diffusion mass-transport should be sufficient to supply the substrate surface with point defects, which are responsible for the inverted behavior. This complements our earlier observation drawn from Stierle's results (71) according to which at 570 K some diffusion in stoichiometric NiAl is already in operation. Note in passing that oxide islands were also observed at the NiAl(100) surface after incomplete oxidation and subsequent annealing at 1200 K (82).

FUTURE STUDIES

Structural Model of the Al₂O₃/NiAl(110) Oxide Film

The atomic structure of the interface between the Al₂O₃ film and the NiAl(110) surface is of major interest. However, even the question as to which of the Al₂O₃ polymorphs corresponds to the structure of the film is still under debate (see

above). Another issue is the atomic structure of the NiAl substrate, including its point defects (71). A number of point defects (oxygen vacancies, for instance) are also suspected in the oxide layer (2). This is exactly the type of problem for which *ab initio* calculations have been helpful. To go beyond the early oxidation calculations described here, the obstacles are largely technical. The oxide film is incommensurate with the substrate, hence a large simulation cell is needed. Otherwise, additional constraints imposed by a small periodic supercell can easily change the structure of alumina and its orientation. Nevertheless, our feeling is that the power of modern computers has reached a level sufficient to tackle the problem. Taking the structural model of Jaeger et al. (24) as a guide, about 200–250 atoms of the substrate and 100 atoms of the oxide film would be a reasonable starting size for the system. We envisage a calculation in which the oxide film is of either γ - or κ -alumina type, and point defects are introduced into the two or three surface layers of the NiAl substrate. The bulk composition of $\text{Ni}_{1-x}\text{Al}_x$ should make its impact indirectly through the Ni and Al chemical potentials, but otherwise it need not be modeled explicitly. Given that even slight deviation from the stoichiometry in ordered alloys affects the composition of their surfaces (83, 84), one might expect the effect to show up in our case as well. In addition, there have recently appeared calculations of free surfaces of $\gamma\text{-Al}_2\text{O}_3$ (85) and $\kappa\text{-Al}_2\text{O}_3$ (86), thus a more comprehensive investigation of NiAl oxidation, or a similar study for other alloys, seems feasible if computationally demanding.

If the atomic structures of the growing oxide film, the substrate, and the interface between them have been established, an even more ambitious project would be a similar study of the boundaries formed between neighboring domains of the oxide film, in which there is much interest at present (67, 87, 88). The observed reflection and antiphase domain boundaries represent the simplest cases of crystal defects, namely special twin grain boundaries and stacking faults, which are straightforward to study in isolation but pose much more difficult problems for simulation where they meet the metal.

Film Thickness

The reason for the original oxide film on NiAl(110) to be exactly 5 Å thick is still a matter of speculation. It cannot be solely because the film, once formed, covers the whole surface and effectively stops the oxidation, for which two Al–O bilayers are sufficient. Indeed, on NiAl(100), the oxide film is twice as thick. It could be reasoned that there is some competition between the chemical energy gain owing to the film formation and the penalty from the elastic energy, which a strained film maintains to remain coherent with the substrate. Indeed, the lattice constants observed for the oxide film are noticeably larger than those in the bulk oxide (by 9.5% and 6.7% compared with bulk γ -alumina (24)). This might explain the dependence of the film thickness on the substrate orientation (the lattice mismatch for the NiAl(100)/ $\gamma\text{-Al}_2\text{O}_3$ interface is only 3% (25)). A refinement of the elastic strain argument is the suggestion that the Madelung energy

in thin two-dimensional films favors larger lattice constants. Thus the thickening of the film leads to an increase in the effective strain. The verification of such apparently reasonable arguments requires ab initio calculations, as the charges on the atoms at surfaces and interfaces do not correspond to their nominal ionic charges (89).

Stability of the Oxide Film

Another intriguing observation is the disappearance of the oxide film at about 1300 K. Is it because of enhanced diffusion, with the film growing so thick that it becomes too expensive to maintain the registry with the substrate, and thus pieces of the film spall? Such an effect is indeed observed during cyclic oxidation experiments. It is usually exploited to prepare a clean NiAl surface, free from impurities (a NiAl sample is heated up to 1500 K and then cooled). However, the alumina film was actually observed to gradually disappear, starting from the step edges, which hints at some sort of thermodynamic instability of the film rather than at any mechanical event (80). This is indeed puzzling because the calculations do not show any signs of the film instability at reported experimental temperature and oxygen partial pressure if static equilibrium is assumed. Resolving this paradox remains a challenge for both theoreticians and experimentalists working on the thermodynamics and kinetics of oxidation. Note in passing that the decomposition of the oxide film at sufficiently high temperature seems to be a rather general effect: It occurs at 1500 K for the Al_2O_3 film on NiAl(100) (90), whereas the Ga_2O_3 film formed on CoGa decomposes at 770 K on the (110) surface (91) and at 850 K on the (100) surface (73).

Free Energy of the Oxidized Surfaces

A significant step forward for simulations of the oxidation process would be a more explicit treatment of the finite temperature effects. Nevertheless, as mentioned above, both the effect of the vibration of substrate atoms and the configurational disorder of bulk point defects would likely be cancelled (to a large extent) if the equivalent amount of bulk material in the expression for the surface energy were subtracted (Equation 4). That is, the remaining effects should be small compared with the gas phase contribution to the free energy. Indeed, according to simple estimations Reference (33) for the RuO_2 (110) surface, the vibrational contribution to the surface energy should not exceed $10 \text{ meV}/\text{\AA}^2$ at temperatures up to 1000 K. Our own surface energy calculations using the quasi-harmonic approximation for Al_2O_3 (0001) indicated a contribution rising to about 10% at 2000 K. Any more detailed study of this important issue is still lacking to our knowledge. We do expect a somewhat larger contribution in less ordered surface structures due to configurational entropy of adsorbed species at relatively low coverages, and owing to the vibration of loosely arranged surface atoms at higher coverages. For the latter, standard harmonic approaches may not be adequate, as the potential energy

surface of such configurations is rich in local minima separated by low barriers. For instance, even during the relatively short MD runs reported here, the A_3 configuration kept jumping between two closely spaced minima (53). For situations like this, the harmonic approximation fails and ab initio MD simulations (92) in combination with thermodynamic integration could be considered instead. Even if simply the entropy S^0 at some reference temperature T^0 could be reasonably estimated in such calculations, a substantial improvement of the estimated Gibbs free energy is expected by adding the linear $(T - T^0)S^0$ term. More generally, systematic studies of the magnitude and relative importance of various contributions to the free energy of an oxidizing substrate up to the coverage of a few monolayers would not only improve the accuracy of estimates of the relative stability of competing surface structures, but, more importantly, would provide general guidance for either neglecting or including particular contributions to the Gibbs free energy of oxidized surfaces.

Other Systems to Study

A large number of first-principles investigations of the oxidation of metallic surfaces have appeared in the past several years, confirming that this important topic is now within the reach of modern ab initio techniques. However, apart from the cited studies of the NiAl(110) surfaces (40, 53), these studies have been restricted to the oxidation of elemental crystals. As we have seen for NiAl, oxidation of multicomponent systems is a much more complex issue, the main principles of which we are just beginning to understand. It is also a rather common situation in practice. Any attempt to look at other systems would therefore be of interest, to see which of the discussed features are common, and which are peculiar to the oxidation of NiAl(110).

An immediate example would be the oxidation of the other low-index surfaces of NiAl, (100) and (111). Both surfaces can be either Ni- or Al-terminated, unlike the (110) surface, which contains half Al and half Ni sites. Hence, the composition of the bulk alloy (either Ni-rich, or Al-rich) may be even more important for such non-stoichiometric faces. A peculiar property of the oxidized NiAl(100) surface is that the structure of the thin Al_2O_3 film formed is highly sensitive to temperature. It is twice as thick as the (110) surface and proceeds through several allotropic modifications with temperature before disappearing at 1500 K (90). NiAl(111) upon oxidation at 1100–1200 K forms (110) facets. The oxide film is found to be located on the (110) surfaces of these facets, whereas (111) terraces remain oxide free. Upon further annealing at higher temperatures (1500 K), the (111) surface becomes flat again (67). The ab initio approach may throw light on the mechanism behind this delicate interplay of surface energies. CoAl, FeAl, and CoGa are among other high-temperature-ordered intermetallic compounds that exhibit selective oxidation and have been extensively studied experimentally (see 67, 72 and references therein). It would be interesting to see whether the surface energies in these compounds depend on oxygen coverage in the same inverted way

as they do for NiAl(110), and whether the transition from layer-by-layer to island growth occurs if point defects are allowed to arrive from the substrate. Characteristic temperatures used for initial oxygen deposition and subsequent annealing steps vary quite significantly from one system to another, which might be helpful in decoupling the bulk diffusion and film-ordering events.

A valuable next step toward the theory of the oxidation of ordered multicomponent crystals would be a study of binary systems in which both components form oxides at comparable rates. TiAl might be an interesting and rather rich system for such an investigation. Upon oxidation, Al_2O_3 and various Ti oxides are formed depending on the oxidation conditions and the composition of the substrate (see, e.g., 93).

CONCLUSIONS

Oxidation of NiAl is a complex process, characterized by the strong interaction of oxygen with Al and the highly ordered nature of the alloy with its characteristic point defect structure. We have described a theoretical framework within which the surface energy of an ordered, but not necessarily stoichiometric, compound can be calculated as a function of external variables defining the state of the system (environmental parameters). The parameters are the temperature, composition of the substrate, and partial pressure of oxygen, with an emphasis in particular on how the surface energy dependence on the environmental parameters can be well approximated with simple analytical expressions.

Oxidation of NiAl proceeds through the arrival and re-arrangement of point defects in the substrate, the ultimate goal of which is to expose Al atoms to oxygen at the oxide-substrate interface and to transport Ni atoms away from it. This is done by exchanging Ni and Al atoms between the surface and subsurface layers and by absorbing Ni vacancies from the bulk. Thus vacancy injection into the substrate is unlikely to occur during the initial stages of the oxidation. On the contrary, the vacancies must be consumed at the oxide-substrate interface. Vacancy injection, however, might be possible at a later stage, after a mature oxide film has been formed through which Al atoms diffuse out to form more oxide. Our oxidation scenario is thus an extended version of the one suggested by Jaeger et al. (24), namely, the initial 5 Å-thick oxide film replaces the two outermost layers of the NiAl(110), whereas Ni atoms dissolve in the bulk and are partially replaced by Al; the latter together with the Al atoms from the two surface layers combine with oxygen to form the Al_2O_3 film.

The 5 Å-thick oxide film is not in thermodynamic equilibrium under most experimental conditions but rather is a transient state in which the system is held by energy barriers. It seems that thermodynamic barriers must be overcome during film formation, in addition to the energy barriers, in order for mass transport to proceed. These thermodynamic barriers are expected to be larger for Ni-rich than for Al-rich NiAl.

Some such thermodynamic barriers are a consequence of the inverted dependence of the surface energy σ on coverage: Under conditions where the surface with a particular coverage becomes stable, a surface with a higher coverage has an even lower energy. The opposite, normal type of behavior, is characterized by a monotonic increase in the adsorbed oxygen with p_{O_2} . We showed that because of the linear dependence of σ on $\log p_{\text{O}_2}$ (the ideal gas assumption), the inverted behavior of surface energies means the convexity of the dependence of surface energy on oxygen coverage. This implies that the differential binding energy of oxygen increases with coverage. The reason lies in the strong interaction between oxygen and aluminum atoms: Increasing, locally, the concentration of oxygen atoms enables them to create a more favorable local environment of aluminum. This, in turn, favors the oxide film growing as separate islands rather than as a uniform layer. Our calculations reveal an interesting link between the dependence of σ on coverage and the point defect mechanism of oxidation. An inverted behavior is observed as long as point defects are allowed in the immediate substrate. If, on the contrary, the immediate substrate is forced to stay perfect, then the surface energies depend on the coverage in a normal way. In other words, constraining the substrate to remain defect-free is sufficient to reduce dramatically the cooperative effect between the oxygen atoms. Whether this is typical for selective oxidation in ordered compounds or peculiar to NiAl is not yet clear. We look forward to calculations on other systems that could clarify this point.

This picture of NiAl oxidation rationalizes a large body of experimental data. For instance, we now understand how the study of lattice point defects in the top substrate layers, on the one hand, and monitoring the oxide growth on the other hand, are looking at two sides of the same coin, namely, whether particular experimental conditions are sufficient to activate mass transport, mediated by point defects, in the bulk NiAl. This idea can be used to clarify why the established procedure to grow a thin alumina film with a well-controlled thickness is such as it is. Because no oxide islands were observed during the initial oxygen deposition at 600 K (80), we conclude that at this temperature the point defect mobility is too low to invert the dependence of surface energy on coverage, which would induce the island growth mode. This means that the type and number of point defects created at and near the substrate surface are not thermodynamically optimal. Subsequent high-temperature annealing, provided that it is long enough and/or the temperature is sufficiently high, removes this constraint. The difference in the annealing temperature might thus explain the apparent discrepancy between the similar studies (71) and (79) regarding the presence of lattice defects in the top substrate layer. The normal behavior of the surface energies is what is needed at the initial deposition stage to produce a uniform layer of adsorbed oxygen atoms that will later be converted into an ordered film. Therefore, raising the temperature at this stage is undesirable because further enhancement of the point defect mobility may induce the island growth mode. Decreasing the deposition temperature, on the other hand, would be unfavorable for a different reason. We recall here the experiment of

Isern & Castro (94), showing that during room temperature oxidation, the oxygen uptake saturates after 90 L exposure. If this is insufficient to build a 5 Å alumina film during the annealing stage, we can understand why low-temperature oxygen deposition results in a different oxide structure (71) and why the reduced dose of oxygen at 600 K leads to similar consequences (80). The reason for this early saturation of oxygen coverage may be that even the near-surface exchanges of Ni and Al necessary for further uptake of oxygen are too slow at room temperature. The existence of an optimal temperature with respect to the quality of the oxide film has been confirmed in experimental work by Lay et al. (70).

We are far from pretending to having reached an exhaustive description of the mechanism of the initial oxidation of NiAl. Surely, many points can also be elucidated by future experimental studies. However, we believe that the NiAl case study is a good illustration of how ab initio calculations, despite their limitations, can provide useful insight even into such a complex issue as the selective oxidation of ordered compounds.

**The Annual Review of Materials Research is online at
<http://matsci.annualreviews.org>**

LITERATURE CITED

1. Miracle DB. 1993. The physical and mechanical properties of NiAl. *Acta Metall. Mater.* 41:649–84
2. Bäumer M, Freund H-J. 1999. Metal deposits on well-ordered oxide films. *Prog. Surf. Sci.* 61:127–98
3. Voter AF, Montalenti F, Germann TC. 2002. Extending the time scale in atomistic simulation of materials. *Annu. Rev. Mater. Res.* 32:321–46
4. Ciacchi LC, Payne MC. 2004. “Hot-Atom” O₂ dissociation and oxide nucleation on Al(111). *Phys. Rev. Lett.* 92:176104
5. Stampf C, Scheffler M. 1996. Theoretical study of O adlayers on Ru(0001). *Phys. Rev. B* 54:2868–72
6. Reuter K, Ganduglia-Pirovano MV, Stampf C, Scheffler M. 2002. Metastable precursors during the oxidation of the Ru(0001) surface. *Phys. Rev. B* 65:165403
7. Ganduglia-Pirovano MV, Scheffler M. 1999. Structural and electronic properties of chemisorbed oxygen on Rh(111). *Phys. Rev. B* 59:15533–43
8. Bocquet M-L, Michaelides A, Sautet P, King DA. 2003. Initial stages in the oxidation and reduction of the 4 × 4 surface oxide phase on Ag{111}: A combined density-functional theory and STM simulation study. *Phys. Rev. B* 68:075413
9. Li W-X, Stampf C, Scheffler M. 2003. Sub-surface oxygen and surface oxide formation at Ag(111): A density-functional theory investigation. *Phys. Rev. B* 67:045408
10. Li W-X, Stampf C, Scheffler M. 2003. Insights into the function of silver as an oxidation catalyst by ab initio atomistic thermodynamics. *Phys. Rev. B* 68:165412
11. Gustafson J, Mikkelsen A, Borg M, Lundgren E, Köhler L, et al. 2004. Self-Limited Growth of a Thin Oxide Layer on Rh(111). *Phys. Rev. Lett.* 92:126102
12. Li WX, Österlund L, Vestergaard EK, Vang RT, Matthiesen J, et al. 2004. Oxidation of Pt(110). *Phys. Rev. Lett.* 93:146104
13. Lundgren E, Kresse G, Klein C, Borg M, Andersen JN, et al. 2002. Two-dimensional oxide on Pd(111). *Phys. Rev. Lett.* 88:246103
14. Lundgren E, Gustafson J, Mikkelsen A,

- Andersen JN, Stierle A, et al. 2004. Kinetic hindrance during the initial oxidation of Pd(100) at ambient pressures. *Phys. Rev. Lett.* 92:046101
15. Todorova M, Li WX, Ganduglia-Pirovano MV, Stampfl C, Reuter K, Scheffler M. 2002. Role of subsurface oxygen in oxide formation at transition metal surfaces. *Phys. Rev. Lett.* 89:096103
16. Schröder E, Fasel R, Kiejna A. 2004. O adsorption and incipient oxidation of the Mg(0001) surface. *Phys. Rev. B* 69:115431
17. Schröder E, Fasel R, Kiejna A. 2004. Mg(0001) surface oxidation: a two-dimensional oxide phase. *Phys. Rev. B* 69:193405
18. Kiejna A, Lundqvist BI. 2001. First-principles study of surface and subsurface O structures at Al(111). *Phys. Rev. B* 63:085405
19. Kiejna A. 2003. Vacancy formation and O adsorption at the Al(111) surface. *Phys. Rev. B* 68:235405
20. Tang H, van der Ven A, Trout BL. 2004. Phase diagram of oxygen adsorbed on platinum(111) by first-principles investigation. *Phys. Rev. B* 70:045420
21. Bongiorno A, Pasquarello A. 2004. Reaction of the oxygen molecule at the Si(100)-SiO₂ interface during silicon oxidation. *Phys. Rev. Lett.* 93:086102
22. Nash P, Kleppa O. 2001. Composition dependence of the enthalpies of formation of NiAl. *J. Alloys Comp.* 321:228–31
23. Lide DR, ed. 1995. *CRC Handbook of Chemistry and Physics*. Boca Raton, FL: CRC Press. 75th ed.
24. Jaeger RM, Kuhlbeck H, Freund H-J, Wuttig M, Hoffmann W, et al. 1991. Formation of a well-ordered aluminium oxide overlayer by oxidation of NiAl(110). *Surf. Sci.* 259:235–52
25. Yang JC, Schumann E, Müllejans H, Rühle M. 1996. Chemistry and bonding investigations of NiAl/ γ -Al₂O₃ interfaces. *J. Phys. D* 29:1716–24
26. Reuter K, Scheffler M. 2003. First-principles atomistic thermodynamics for oxidation catalysis: surface phase diagrams and catalytically interesting regions. *Phys. Rev. Lett.* 90:046103
27. Zhang W, Smith JR, Wang X-G. 2004. Thermodynamics from ab initio computations. *Phys. Rev. B* 70:024103
28. Bergermayer W, Schweiger H, Wimmer E. 2004. Ab initio thermodynamics of oxide surfaces: O₂ on Fe₂O₃(0001). *Phys. Rev. B* 69(19):195409
29. Rogal J, Reuter K, Scheffler M. 2004. Thermodynamic stability of PdO surfaces. *Phys. Rev. B* 69:075421
30. Wang X-G, Smith JR. 2003. Surface phase diagram for Cr₂O₃(0001): ab initio density functional study. *Phys. Rev. B* 68:201402
31. Ganduglia-Pirovano MV, Sauer J. 2004. Stability of reduced V₂O₅(001) surfaces. *Phys. Rev. B* 70:045422
32. Meyer B. 2004. First-principles study of the polar O-terminated ZnO surface in thermodynamic equilibrium with oxygen and hydrogen. *Phys. Rev. B* 69:045416
33. Reuter K, Scheffler M. 2002. Composition, structure, and stability of RuO₂(110) as a function of oxygen pressure. *Phys. Rev. B* 65:035406
34. Batyrev IG, Alavi A, Finnis MW. 2000. Equilibrium and adhesion of Nb/sapphire: the effect of oxygen partial pressure. *Phys. Rev. B* 62:4698–706
35. Wang X-G, Chaka A, Scheffler M. 2000. Effect of the environment on α -Al₂O₃(0001) surface structures. *Phys. Rev. Lett.* 84:3650–53
36. Lodziana Z, Nørskov JK, Stoltze P. 2003. The stability of the hydroxylated (0001) surface of α -Al₂O₃. *J. Chem. Phys.* 118:11179–88
37. Wang X-G, Smith JR. 2004. Hydrogen and carbon effects on Al₂O₃ surface phases and metal deposition. *Phys. Rev. B* 70:081401
38. Marmier A, Parker SC. 2004. Ab initio morphology and surface thermodynamics of α -Al₂O₃. *Phys. Rev. B* 69:115409
39. Cahn JW. 1978. Thermodynamics of solid and fluid surfaces. In *Interfacial*

- Segregation*, ed. WC Johnson, JM Blakely, pp. 3–23. Ohio: ASM
40. Lozovoi AY, Alavi A, Finnis MW. 2000. Surface stoichiometry and the initial oxidation of NiAl(110). *Phys. Rev. Lett.* 85:610–13
 41. Johnston K, Castell MR, Paxton AT, Finnis MW. 2004. SrTiO₃(001) (2 × 1) reconstructions: first-principles calculations of surface energy and atomic structure compared with scanning tunneling microscopy images. *Phys. Rev. B* 70:085415
 42. Finnis MW. 1998. Accessing the excess: an atomistic approach to excesses at planar defects and dislocations in ordered compounds. *Phys. Stat. Solidi* 166:397–416
 43. Xie J, de Gironcoli S, Baroni S, Scheffler M. 1999. Temperature-dependent surface relaxations of Ag(111). *Phys. Rev. B* 59:970–74
 44. Marzari N, Vanderbilt D, de Vita A, Payne MC. 1999. Thermal contraction and disordering of the Al(110) Surface. *Phys. Rev. Lett.* 82:3296–99
 45. Lazzeri M, de Gironcoli S. 2002. First-principles study of the thermal expansion of Be(1010). *Phys. Rev. B* 65:245402
 46. Wagner C, Schottky W. 1930. Theorie der geordneten Mischphasen. *Z. Phys. Chem. B* 11:163–210
 47. Hagen M, Finnis MW. 1998. Point defects and chemical potentials in ordered alloys. *Philos. Mag. A* 77:447–64
 48. Meyer B, Fähnle M. 1999. Atomic defects in the ordered compound B2-NiAl: a combination of ab initio electron theory and statistical mechanics. *Phys. Rev. B* 59:6072–82
 49. Korzhavyi PA, Ruban AV, Lozovoi AY, Vekilov YuKh, Abrikosov IA, Johansson B. 2000. Constitutional and thermal point defects in B2 NiAl. *Phys. Rev. B* 61:6003–18
 50. Mishin Y, Herzig C. 2000. Diffusion in the Ti-Al system. *Acta Mater.* 48:589–623
 51. Qian G, Martin RM, Chadi DJ. 1988. Stoichiometry and surface reconstruction: an ab initio study of GaAs(100) surfaces. *Phys. Rev. Lett.* 60:1962–65
 52. Zhang SB, Northrup JE. 1991. Chemical potential dependence of defect formation energies in GaAs: application to Ga self-diffusion. *Phys. Rev. Lett.* 67:2339–42
 53. Lozovoi AY, Alavi A, Finnis MW. 2001. Surface energy and the early stages of oxidation of NiAl(110). *Comput. Phys. Commun.* 137:174–94
 54. Linstrom PJ, Mallard WG, eds. 2003. *NIST Chemistry Web Book, NIST Standard Reference Database Number 69*. Gaithersburg, MD: Natl. Inst. Standard. Technol., <http://webbook.nist.gov>
 55. Cox JD, Wagman DD, Medvedev VA. 1989. *CODATA Key Values for Thermodynamics*. New York: Hemisphere
 56. JANAF Thermochemical Tables. 1974. Suppl. 1974. *J. Phys. Chem. Ref. Data* 3
 57. JANAF Thermochemical Tables. 1975. Suppl. 1975. *J. Phys. Chem. Ref. Data* 4
 58. Bradley AJ, Taylor A. 1937. An X-ray analysis of the nickel-aluminium system. *Proc. R. Soc. London Ser. A* 159:56–72
 59. Fu CL, Ye Y-Y, Yoo MH, Ho KM. 1993. Equilibrium point defects in intermetallics with the B2 structure: NiAl and FeAl. *Phys. Rev. B* 48:6712–15
 60. Alavi A, Lozovoi AY, Finnis MW. 1999. Pressure-induced isostructural phase transition in Al-rich NiAl alloys. *Phys. Rev. Lett.* 83:979–82
 61. Desai PD. 1987. Thermodynamic properties of selected binary aluminum alloy systems. *J. Phys. Chem. Ref. Data* 16:109–24
 62. In calculating the ab initio curves for p_n and p_s shown in Figure 3, we have employed an additional thermodynamic cycle that allowed us to circumvent explicit calculations of Ni(fcc) and NiO crystals (see Reference 53 for details).
 63. Brandes EA, Brook GB, eds. 1992. *Smithells Metals Reference Book*. Oxford, UK: Butterworth-Heinemann. 7th ed.
 64. Ustundag E, Clausen B, Bourke MAM. 2000. Neutron diffraction study of the reduction of NiAl₂O₄. *Appl. Phys. Lett.* 76:694–96

65. Elrefaie FA, Smeltzer WW. 1981. Thermodynamics of nickel-aluminum-oxygen system between 900 and 1400 K. *J. Electrochem. Soc.* 128:2237–42
66. Doychak J, Smialek JL, Mitchell TE. 1989. Transient oxidation of single-crystal β -NiAl. *Metall. Trans. A* 253:499–518
67. Franchy R. 2000. Growth of thin, crystalline oxide, nitride and oxynitride films on metal and metal alloy surfaces. *Surf. Sci. Rep.* 38:195–294
68. Stierle A, Renner F, Streitel R, Dosch H, Drube W, Cowie BC. 2004. X-ray diffraction study of the ultrathin Al_2O_3 layer on NiAl(110). *Science* 303:1652–56
69. Yoshitake M, Mebarki B, Lay TT. 2002. Crystallinity and thickness control of well-ordered ultra-thin Al_2O_3 film on NiAl(110). *Surf. Sci.* 511:L313–18
70. Lay TT, Yoshitake M, Mebarki B. 2002. Temperature effect on growth of well-ordered thin Al_2O_3 film on NiAl(110). *J. Vac. Sci. Technol. A* 20:2027–31
71. Stierle A, Renner F, Streitel R, Dosch H. 2001. Observation of bulk forbidden defects during the oxidation of NiAl(110). *Phys. Rev. B* 64:165413
72. Rose V, Podgursky V, Costina I, Franchy R. 2003. Growth of ultra-thin amorphous Al_2O_3 films on CoAl(100). *Surf. Sci.* 541:128–36
73. Pan FM, Pflitsch C, David R, Verheij LK, Franchy R. 2001. Formation of an ordered oxide on the CoGa(100) surface by room temperature oxidation and annealing. *Surf. Sci.* 479:191–200
74. Frazer HL, Loretto MH, Smallman RE, Wasilewski RJ. 1973. Oxidation-induced defects in NiAl. *Philos. Mag.* 28:639–50
75. Eibner JE, Engell H-J, Schultz H, Jakobi H, Schlatter G. 1975. Annealing of point defects in quenched NiAl. *Philos. Mag.* 31:739–42
76. Parthasarathi A, Frazer HL. 1984. The annealing of vacancy defects in β -NiAl. II. The role of surface oxidation in vacancy loop growth in slowly cooled crystals. *Philos. Mag. A* 50:101–15
77. Some results presented in Reference 40 were misinterpreted in Reference 71, suggesting that there is a discrepancy between the results of these studies. The authors of the latter paper took the composition of the top layer in configuration E_3 as a prediction for the defect structure of the first substrate layer. However in Reference 40, the layer in question was treated as part of the oxide film, not the substrate. Also, in Reference 40, the defect concentration was not optimized in any layer, as the supercell is far too small for that. Thus there is actually no discrepancy between the results of the two studies.
78. McCarty KF, Nobel JA, Bartelt NC. 2001. Vacancies in solids and the stability of surface morphology. *Nature* 412:622–25
79. Torrelles X, Wendler F, Bikondoa O, Isern H, Moritz W, Castro GR. 2001. Structure of the clean NiAl(110) surface and the Al_2O_3 /NiAl(110) interface by measurements of crystal truncation rods. *Surf. Sci.* 487:97–106
80. McCarty KF. 2001. Imaging the crystallization and growth of oxide domains on the NiAl(110) surface. *Surf. Sci.* 474:L165–72
81. Ceballos G, Song Z, Pascual JI, Rust H-P, Conrad H. 2002. Structure investigation of the topmost layer of a thin ordered alumina film grown on NiAl(110) by low temperature scanning tunneling microscopy. *Chem. Phys. Lett.* 359:41–47
82. Blum R-P, Ahlbehrendt D, Niehus H. 1998. Growth of Al_2O_3 stripes in NiAl(001). *Surf. Sci.* 396:176–88
83. Ruban AV. 2002. Surface composition of ordered alloys: An off-stoichiometric effect. *Phys. Rev. B* 65:174201
84. Blum V, Hammer L, Schmidt C, Meier W, Wieckhorst O, et al. 2002. Segregation in strongly ordering compounds: a key role of constitutional defects. *Phys. Rev. Lett.* 89:266102
85. Pinto HP, Nieminen RM, Elliott SD. 2004. Ab initio study of γ - Al_2O_3 surfaces. *Phys. Rev. B* 70:125402
86. Ruberto C, Yourdshahyan Y, Lundqvist BI.

2003. Surface properties of metastable alumina: a comparative study of κ - and α - Al_2O_3 . *Phys. Rev. B* 67:195412
87. Kulawik M, Nilius N, Rust H-P, Freund H-J. 2003. Atomic structure of antiphase domain boundaries of a thin Al_2O_3 film on $\text{NiAl}(110)$. *Phys. Rev. Lett.* 91:256101
88. Nilius N, Kulawik M, Rust H-P, Freund H-J. 2004. Defect-induced gap states in Al_2O_3 thin films on $\text{NiAl}(110)$. *Phys. Rev. B* 69:121401
89. Finnis MW. 1999. Why is $\text{InSb}(111)$ reconstructed? *CCP3 Newslett.* 24:2–11. <http://www.Ccp3.Ac.uk/newsletters.Shtml>
90. Gassmann P, Franchy R, Ibach H. 1994. Investigation on phase transitions within thin Al_2O_3 layers on $\text{NiAl}(001)$ —HREELS on aluminium oxide films. *Surf. Sci.* 319:95–109
91. März A, Franchy R. 2000. Oxidation of $\text{CoGa}(110)$. *Surf. Sci.* 466:54–65
92. Walker BG, Molteni C, Marzari N. 2004. Ab initio molecular dynamics of metal surfaces. *J. Phys. Condens. Matter* 16:S2575–96
93. Schmiedgen M, Graat PCJ, Baretzky B, Mittemeijer EJ. 2002. The initial stages of oxidation of γ - TiAl : an X-ray photoelectron study. *Thin Solid Films* 415:114–22
94. Isern H, Castro GR. 1989. The initial interaction of oxygen with a $\text{NiAl}(110)$ single crystal: a LEED and AES study. *Surf. Sci.* 211/212:865–71

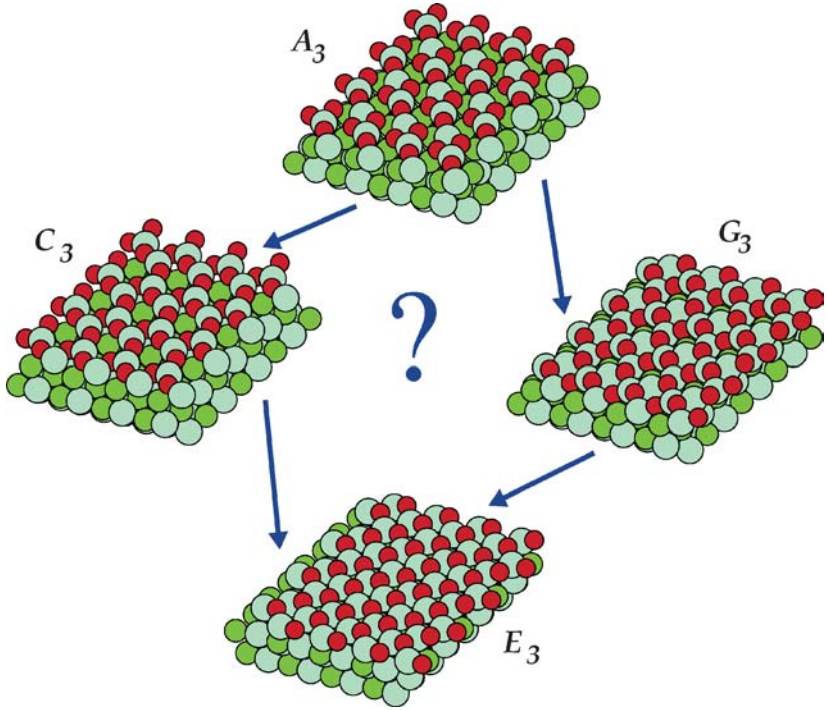


Figure 4 The optimized atomic structure of the most characteristic configurations corresponding to 0.75 ML oxygen coverage. Oxygen atoms are shown in red, Al atoms in cyan, and Ni atoms in green. Configuration A_3 corresponds to the perfect NiAl(110) substrate, configuration C_3 contains a Ni vacancy in the top layer, $V_{Ni}^{(1)}$, configuration G_3 contains the exchange defect, $Ni_{Al}^{(2)} + Al_{Ni}^{(1)}$, and configuration E_3 contains both defects (see Table 2 for the notation). At a fixed O coverage of 0.75 ML, the oxidation begins with A_3 and proceeds to E_3 through C_3 and/or G_3 .

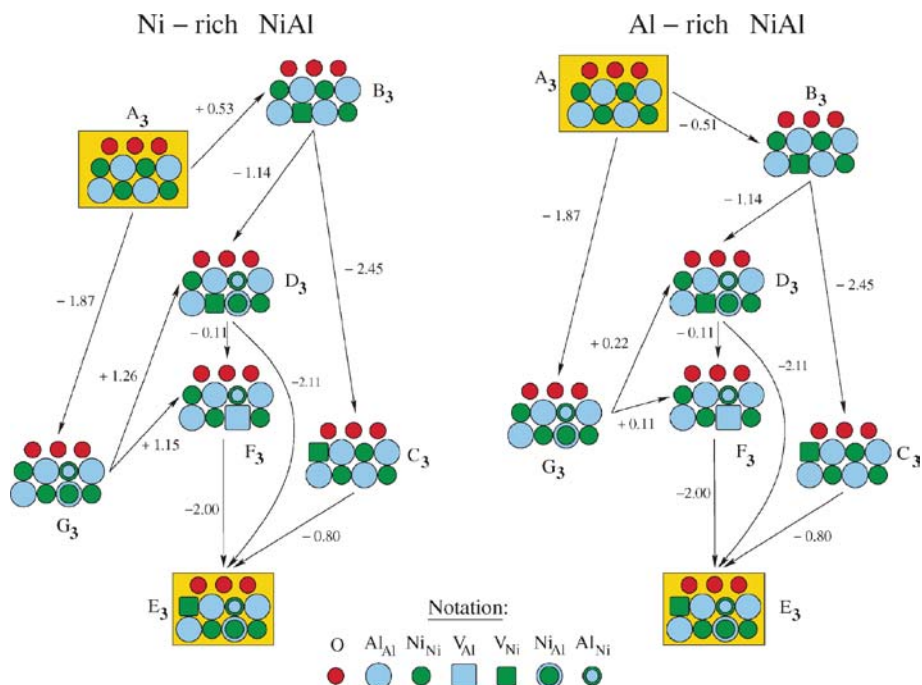


Figure 5 Pathways for point defect-mediated optimization of the structure of the surface oxide at NiAl(110) at fixed oxygen coverage of 1 ML starting from the defect-free substrate, configuration A_3 , and finishing in configuration E_3 containing a Ni vacancy in the top layer, $V_{Ni}^{(1)}$, and the exchange defect, $Ni_{Al}^{(2)} + Al_{Ni}^{(1)}$. Configurations are labeled as in Table 2. The energy changes at each single-step event are given in eV. The difference between the Ni-rich and Al-rich systems enters through the chemical potential of the components, Equations (22)–(25), taken at zero Kelvin.

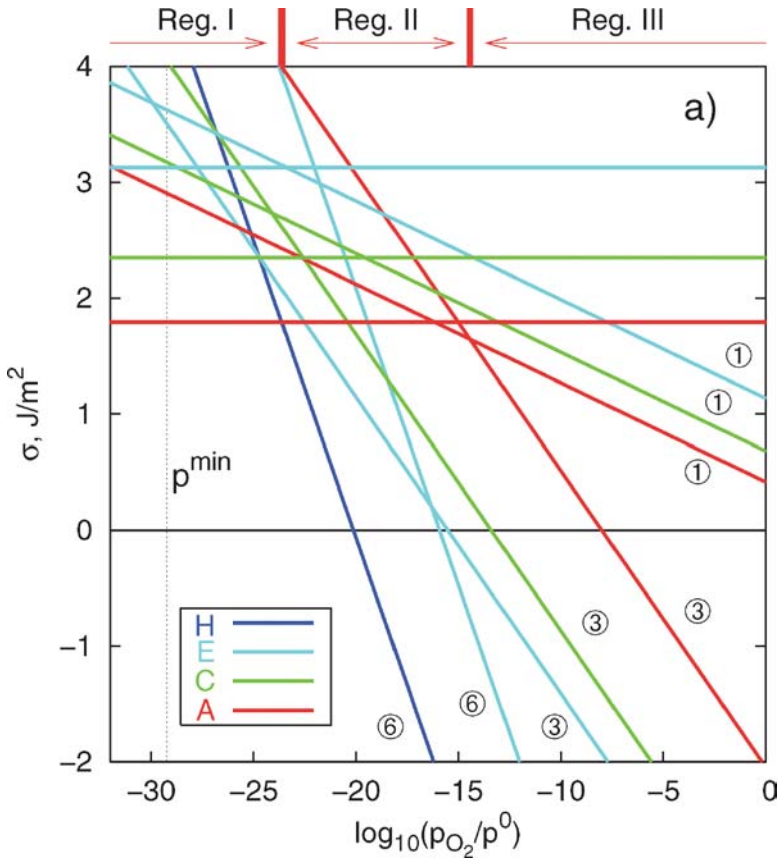


Figure 6 Surface energy σ , Equation (26), of configurations A (red lines), C (green lines), E (light blue lines), and H (dark blue lines) as a function of the oxygen partial pressure p_{O_2} at $T = 1273$ K: (a) assuming the bulk composition of the substrate $\text{Ni}_{0.55}\text{Al}_{0.45}$; (b, overleaf) assuming the bulk composition of the substrate $\text{Ni}_{0.45}\text{Al}_{0.55}$. The thin vertical dotted line indicates the stability limit of bulk $\alpha\text{-Al}_2\text{O}_3$ in contact with NiAl, Equation (31). Horizontal lines correspond to the $\Gamma_{\text{O}A_s} = 0$ family; lines corresponding to $\Gamma_{\text{O}A_s} = 1, 3,$ and 6 are marked with the respective numbers; to convert to oxygen coverage in monolayers, these should be divided by 3. Oxidation regions: I (clean surface), II (oxidation with additional barriers), and III (down-hill oxidation) are indicated above the plot.

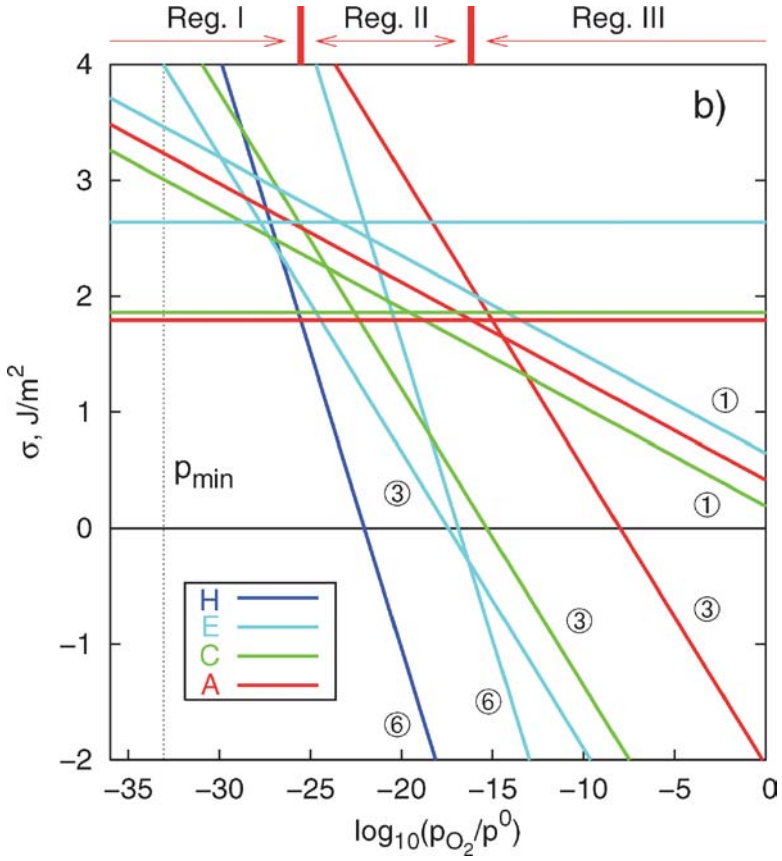


Figure 6 (Continued)



CONTENTS

MATERIALS DESIGN AND CHEMISTRY OF ENVIRONMENTALLY ACCEPTABLE CATALYSTS

- THE PREPARATION AND CHARACTERIZATION OF HIGHLY EFFICIENT
TITANIUM OXIDE–BASED PHOTOFUNCTIONAL MATERIALS,
*Masakazu Anpo, Satoru Dohshi, Masaaki Kitano, Yun Hu,
Masato Takeuchi, and Masaya Matsuoka* 1
- APPLICATION OF EXAFS TO MOLTEN SALTS AND IONIC LIQUID
TECHNOLOGY, *Christopher Hardacre* 29
- THE PREPARATION OF SKELETAL CATALYSTS, *A.J. Smith and D.L. Trimm* 127
- HETEROGENEOUS ASYMMETRIC CATALYSTS: STRATEGIES FOR ACHIEVING
HIGH ENANTIOSELECTION, *Graham J. Hutchings* 143
- ENGINEERED POROUS CATALYTIC MATERIALS, *Ferdi Schüth* 209
- DESIGNING CATALYSTS FOR CLEAN TECHNOLOGY, GREEN CHEMISTRY,
AND SUSTAINABLE DEVELOPMENT, *John Meurig Thomas
and Robert Raja* 315
- POROUS ALUMINOPHOSPHATES: FROM MOLECULAR SIEVES TO DESIGNED
ACID CATALYSTS, *H.O. Pastore, S. Coluccia, and L. Marchese* 351
- CHEMICAL DESIGN AND IN SITU CHARACTERIZATION OF ACTIVE
SURFACES FOR SELECTIVE CATALYSIS, *Mizuki Tada
and Yasuhiro Iwasawa* 397
- METAL CATALYST DESIGN AND PREPARATION IN CONTROL OF
DEACTIVATION, *Michael S. Spencer and Martyn V. Twigg* 427
- ELECTRON MICROSCOPY IN THE CATALYSIS OF ALKANE OXIDATION,
ENVIRONMENTAL CONTROL, AND ALTERNATIVE ENERGY SOURCES,
Pratibha L. Gai and Jose J. Calvino 465

CURRENT INTEREST

- THE DIFFUSION–MULTIPLE APPROACH TO DESIGNING ALLOYS,
Ji-Cheng (J.-C.) Zhao 51
- SPATIAL ORDER AND DIFFRACTION IN QUASICRYSTALS AND BEYOND,
Denis Gratias, Lionel Bresson, and Marianne Quiquandon 75

INFLUENCE OF INTERFACE ANISOTROPY ON GRAIN GROWTH AND COARSENING, <i>Gregory S. Rohrer</i>	99
THE OXIDATION OF NiAl: WHAT CAN WE LEARN FROM AB INITIO CALCULATIONS? <i>M.W. Finnis, A.Y. Lozovoi, and A. Alavi</i>	167
ANALYTICAL TRANSMISSION ELECTRON MICROSCOPY, <i>Wilfried Sigle</i>	239
COMPOSITE MATERIALS FOR WIND POWER TURBINE BLADES, <i>Povl Brøndsted, Hans Lilholt, and Aage Lystrup</i>	505
MATERIALS CHARACTERIZATION IN THE ABERRATION-CORRECTED SCANNING TRANSMISSION ELECTRON MICROSCOPE, <i>M. Varela, A.R. Lupini, K. van Benthem, A.Y. Borisevich, M.F. Chisholm, N. Shibata, E. Abe, and S.J. Pennycook</i>	539
ADHESION AND DE-ADHESION MECHANISMS AT POLYMER/METAL INTERFACES: MECHANISTIC UNDERSTANDING BASED ON IN SITU STUDIES OF BURIED INTERFACES, <i>G. Grundmeier and M. Stratmann</i>	571

INDEXES

Subject Index	617
Cumulative Index of Contributing Authors, Volumes 31–35	655
Cumulative Index of Chapter Titles, Volumes 31–35	657

ERRATA

An online log of corrections to *Annual Review of Materials Research* chapters may be found at <http://matsci.annualreviews.org/errata.shtml>